Materials Reports: Energy 2 (2022) 100141

Contents lists available at ScienceDirect

Materials Reports: Energy

journal homepage: www.keaipublishing.com/en/journals/materials-reports-energy

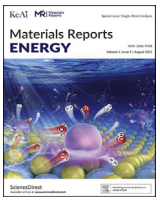

Review

Fe–N–C single atom catalysts for the electrochemical conversion of carbon, nitrogen and oxygen elements

Jian Huang [a,1], Qiao Zhang [a,1], Jie Ding [a,b,**], Yueming Zhai [a,*]

[a] The Institute for Advanced Studies, Wuhan University, Wuhan, 430072, China
[b] School of Chemical and Biomedical Engineering, Nanyang Technological University, 62 Nanyang Drive, Singapore, 637459, Singapore

ARTICLE INFO

Keywords:
Single atom catalysts
Fe–N–C synthesis
Spin
Electrochemical conversion
CO_2 reduction reaction
Nitrogen reduction reaction
Oxygen reduction reaction

ABSTRACT

Single atom catalysts (SACs) are constituted by isolated active metal centers, which are heterogenized on inert supports such as graphene, porous carbon, and amorphous carbon. The thermal stability, electronic properties, and catalytic activities of the metal center can be controlled via manipulating the neighboring heteroatoms such as nitrogen, oxygen, and sulfur. Due to the atomical dispersion of the active catalytic centers, the amount of metal required for catalysis can be decreased. Furthermore, new possibilities are offered to easily control the selectivity of a given transformation process as well as to improve turnover frequencies and turnover numbers of target reactions. Among them, Fe–N–C single atom catalysts own special electronic structure, and have been widely used in many fields of electrocatalysis. This review aims to summarize the synthesis of Fe–N–C based on anchoring individual iron atoms on carbon/graphene. The spin-related properties of Fe–N–C catalysts are described, including the relation between spin and electron structure of Fe–N_x as well as the coupling between electronic structure of Fe–N_x and electronic (orbit) of CO_2, N_2 and O_2. Next, mechanistic investigations conducted to understand the specific behavior of Fe–N–C catalysts are highlighted, including C, N, O electro-reduction. Finally, some issues related to the future developments of Fe–N–C are put forward and corresponding feasible solutions are offered.

1. Introduction

With the rapid development of society, the excessive consumption of fossil fuels and the dramatically increasing of energy demand have caused serious environmental pollution and energy crisis. The development of renewable energy and energy conversion technologies is considered to be an effective way to solve these two issues.[1–6] Especially, electrocatalytic conversion devices composed of electrocatalysts, membrane and electrolytes have attracted extensive attention from researchers because of their high efficiency and cleanliness.[7] However, their large-scale application is greatly limited by the slow kinetics of the cathodic reaction. Therefore, the development of highly active and stable electrocatalysts is necessary to improve energy conversion efficiency of emerging devices and propel their commercialization.

Traditional heterogeneous catalysts (e.g. Pt-based catalysts and RuO_2) usually contain a mixture of metal particles with a wide size distribution. However, only a small fraction of metal particles with appropriate size distribution can be used as catalytically active species, while others are either inert or probable to trigger undesired side reactions, which results in low metal utilization efficiency and poor selectivity of the reaction.[8–10] Homogeneous catalysts have well-structured active sites and tunable ligand environments, which exhibit excellent activity and high selectivity for the target reaction. However, the catalysts still suffer from limitations such as poor stability and unsatisfactory recoverability.[11] Single atom catalysts (SACs) combine the advantages of "isolated sites" from homogeneous catalysts and the structural stability as

* Corresponding author.
** Corresponding author. The Institute for Advanced Studies, Wuhan University, Wuhan, 430072, China.
E-mail addresses: jieding@whu.edu.cn (J. Ding), yueming@whu.edu.cn (Y. Zhai).

Production and Hosting by Elsevier on behalf of KeAi

[1] These authors contributed equally.

https://doi.org/10.1016/j.matre.2022.100141
Received 26 April 2022; Received in revised form 21 June 2022; Accepted 1 July 2022
Available online 20 July 2022

well as convenience of separation from heterogeneous catalysts, which serve as a bridge between homogeneous and heterogeneous catalysts.[12–14]

Since Zhang and coworkers reported single Pt atom on iron oxide for CO oxidation in 2011,[15] single atom catalysts have attracted a lot of attention in various aspects, such as photocatalysis,[16–20] electrocatalysis[21–25] and thermal catalysis[26–28] because of their maximal atom utilization (nearly 100%) and high catalytic activity, stability and selectivity. The size reduction of nanoparticles to the sub-nanometer level leads to an increasing in number of low-coordinated metal atoms that can be used as catalytically active sites, which will be maximized at the single-atom level when individual metal atoms are accessible and catalytically active.[29] However, these low coordination single atoms have very high surface energy and tend to aggregate during the synthesis process.[27] Therefore, it is of great importance to select suitable supports to interact with metal single atoms to prevent their aggregation for the synthesis of single-atom catalysts.[30] Common support materials include metal oxides,[15] metal sulfides,[31] metal nitrides,[32] metal surfaces,[33] MOFs,[34] porous carbon materials,[35,36] g-C_3N_4[37,38] and graphene.[39,40] Among them, nitrogen-doped porous carbon is considered as an ideal single-atom support due to its hierarchical pore structure, high mechanical strength and special defect effect.[14]

Metal-nitrogen-carbon catalysts, in which dispersive metal atoms are coordinated to nitrogen atoms doped in carbon nanomaterials, have been used as effective catalysts for lots of electrochemical reactions, such as carbon dioxide reduction reaction (CO_2RR),[41–44] nitrogen reduction reaction (NRR),[45,46] oxygen reduction reaction (ORR),[47–49] oxygen evolution reaction (OER),[50] hydrogen oxidation reaction (HOR)[51] and hydrogen evolution reaction (HER).[52] Precious metal catalysts show excellent activity for these reactions, but their high cost and low natural abundance have forced the search for suitable metal substitutes. In contrast, iron is well-known to be abundant in nature and inexpensive, and also exhibits high durability, tunability in both acidic and alkaline medium, and methanol tolerance, which has led to many iron-based catalysts being explored for numerous reactions, especially in the reduction of C, N and O.

In this review, as shown in Fig. 1, we firstly conclude several essential methods for the synthesis of Fe–N–C. Then, we present the property of Fe–N–C catalysts, including spin-related interaction of electronic structures as well as the orbital coupling between the electronic structure of Fe–N_x and the electronic orbital of C, N and O. Furthermore, we summarize the electrocatalytic applications about the chemical conversion of C, N and O with Fe–N–C. Lastly, we discuss some challenges in structural characterization, mechanistic investigation and industrial application of Fe–N–C, and propose some possible solutions.

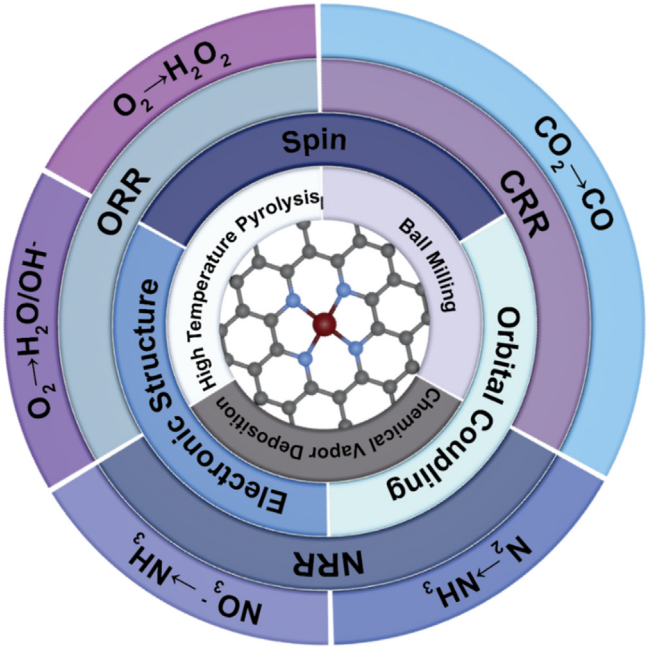

Fig. 1. Schematic illustration of synthetic methods, spin-related properties and electrocatalytic applications of Fe–N–C.

2. Synthesis

2.1. High temperature pyrolysis method

2.1.1. Pyrolysis derived from metal-organic frameworks (MOFs)-based precursors

Since 2008, MOFs have been widely recognized as ideal sacrificial templates for preparing of highly stable and conductive nanostructured carbon.[53] By charring the MOF precursors with the target metals, it was found that the single atoms (SAs) were firmly embedded into the carbon carriers through strong metal heteroatom (S/N/O) coordination bonds, successfully providing single-atom catalysts with excellent catalytic performance.[54] The iron source is first anchored into the networks of the metal nodes and organic linkages, as well as in the cavities of the entire MOF crystal to form iron-containing MOF precursors, which are then converted into Fe SACs in one-step pyrolysis treatment. So far, the most commonly used MOF precursor in this method is a zinc imidazole skeleton doped with a small amount of iron because of its good structural tailorability, high nitrogen content and the pore confinement effect. Under solvent or solvent-free conditions, Fe^{2+}/Fe^{3+} is spatially separated by Zn^{2+} and 2-methylimidazole ligands, which are atomically diluted throughout the MOF crystals. During pyrolysis at high temperatures, Zn metal readily evaporates out of the system due to its low boiling point, leaving the Fe SAs distributed on the MOF-derived porous carbon framework (Fig. 2a).[55] It is worth mentioning that the nitrogen atoms from the organic linkers will firmly anchor and stabilize these Fe single atoms, thus effectively avoiding their migration and aggregation.

To improve the activity of Fe–N–C, Zhang et al. replaced ZIF-8 with MIL-101 to act as a precursor to introduce abundant mesopores (Fig. 2b).[56] However, the iron-containing MIL-101 has high iron content and insufficient nitrogen content, so amino groups are further introduced in preparing of the precursor to reduce the formation of Fe nanoparticles in the catalyst. Firstly, NH_2-MIL-101(Al) was pyrolyzed to obtain nitrogen-doped carbon materials (NC-MIL101-T) at a temperature range of 800–1100 °C under N_2. After acid etching, $Fe(phen)_3^{2+}$ and NC-MIL101-T support were thoroughly mixed. Fe_{SAC}-MIL101-T catalysts were finally obtained after freeze-drying and the second pyrolysis at 800 °C. Later, Yang et al. proposed to replace Zn by Cd as a sacrificial metal for the synthesis of Fe–N–C, which could reduce the pyrolysis temperature of the precursor from 1000 °C to 750 °C and thus help to preserve the individual iron atom active sites. Meanwhile, as a comparison, the ZIF-8/Fe catalyst was prepared by pyrolysis at the same temperature. In contrast to the ZIF-8/Fe catalyst, the Fe–N–C retained a smaller amount of sacrificial metal and formed a higher density of single-atom structures.[59]

In addition, Jiang and co-workers used a hybrid ligand strategy to prepare high-content (1.76 wt%) single-atom iron-implanted nitrogen-doped porous carbon (Fe_{SA}–N–C) by pyrolysis of porphyrinic MOFs (Fe–PCN-222). The mixed porphyrin ligands, Fe-TCPP and H_2-TCPP made the Fe(III) ions form a long spatial distance in the MOF skeleton, which was conducive to the formation of single iron atoms by pyrolysis.[60] Later, Jiang et al. developed a similar strategy to obtain Fe_{SA}–N–C with high Fe loading (3.46%) by the pyrolysis of SiO_2@MOF composite (Fig. 2c).[57] The pre-synthesized PCN-222(Fe) has a one-dimensional pore structure of ~3.2 nm, which ensures that tetraethylorthosilicate (TEOS) can be fully permeable in the internal space. Under hydrochloric acid vapor treatment, TEOS was hydrolyzed and condensed to silica, forming the SiO_2@MOF composite with well-retained MOF crystallinity. Silica

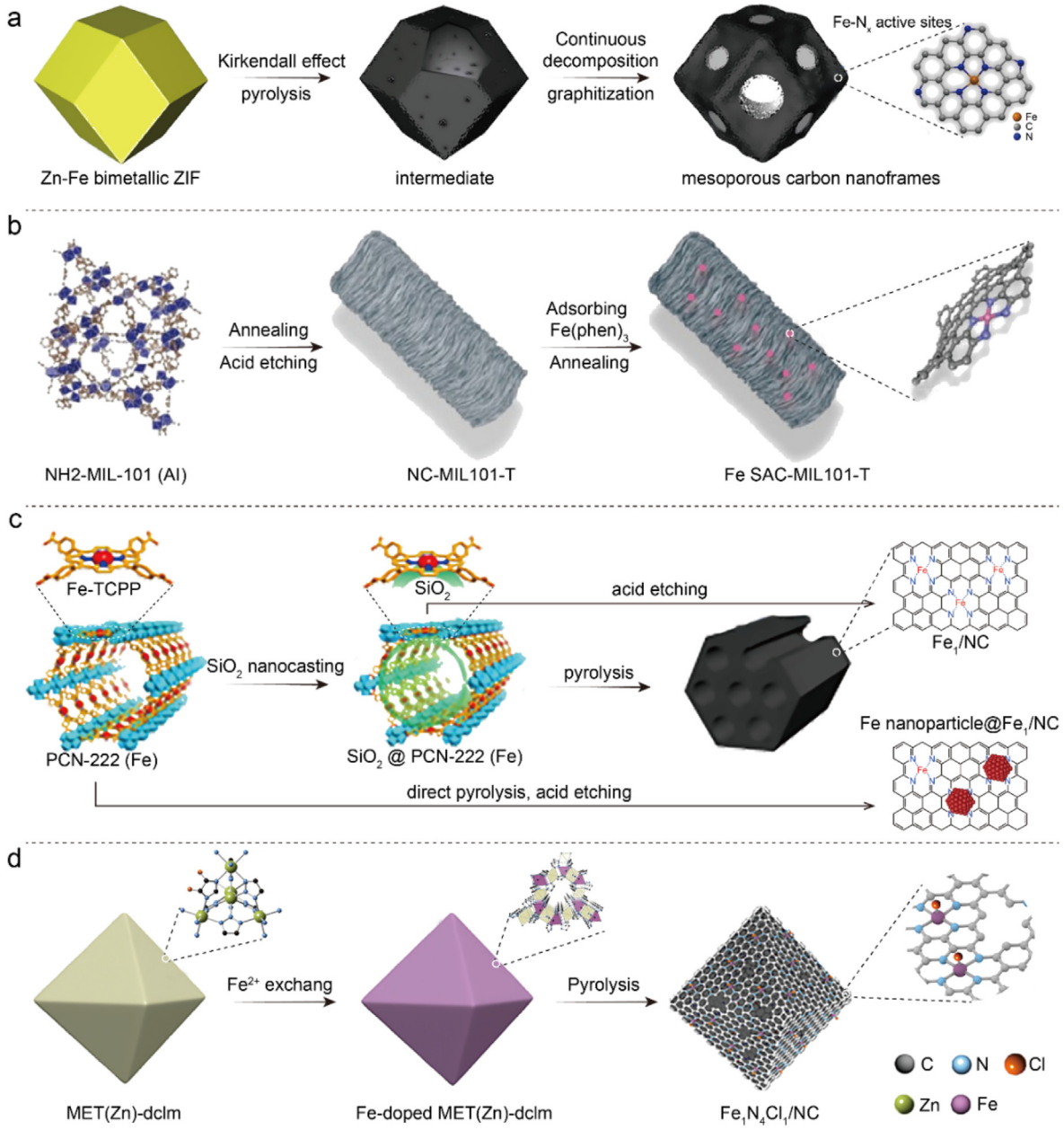

Fig. 2. Schematic illustration of the formation of (a) Fe_{SA}–NC based on ZIF, (b) preparation of Fe SAC-MIL101-T, (c) formation of Fe_{SA}–N–C catalyst by pyrolysis of SiO_2@Fe–PCN-222 composite and direct pyrolysis of Fe–PCN-222, (d) formation of FeN_4Cl_1/NC. Reproduced with permission from (a) Ref. 55, (b) Ref. 56, (c) Ref. 57, (d) Ref. 58.

interacts with iron atoms to increase the energy barrier for iron atoms migration and thus prevent their aggregation. Moreover, the removal of silica increases the porosity and specific surface area of the material, which facilitates the exposure of active sites and mass transfer. In contrast, Fe particles could be detected from the catalyst obtained by the direct pyrolysis of PCN-222(Fe) without SiO_2, which proved that the presence of SiO_2 inhibited the migration of Fe atoms under pyrolysis.

Moreover, heteroatom doping is an important means to increase the density of active centers and improve the electrocatalytic activity of catalysts. The doping of heteroatoms can change the coordination environment and electronic properties of iron centers as well as change the density of active centers through long-range or short-range interactions. Wang et al. designed a Zn/Fe bimetallic mixed-ligand metal-triazolate (MET) as the precursor and 4,5-dichloroimidazole as the source of Cl to obtain FeN_4Cl/NC (Fig. 2d). The higher electronegativity of chlorine could change the d-band delocalization and electronic structure of Fe atoms to ensure the presence of FeN_4Cl coordination configuration.[58]

2.1.2. Pyrolysis derived from irregular metal-containing complexes and polymers

Irregular metal-containing complexes and polymers can replace MOFs as precursors to prepare atomically dispersed Fe–N–C catalysts with special structures via pyrolysis. Tang et al. designed atomically dispersed iron atoms anchored on N-doped carbon nanosheets (Fe–N–C HNSs) with well-defined FeN_4 structures and unique spherical hollow architecture via SiO_2-templated strategy. Histidine (His) served as the source of N and C due to high content of heteroatoms and natural abundance. During the process of preparation, the pre-synthesized SiO_2 nanospheres could absorb Fe^{3+} ions through electrostatic attractions after surface modification with negative charges. Subsequently, the His

molecules bound with Fe^{3+} ions to form SiO_2@Fe-His nanospheres, which would be pyrolyzed at high temperature and acid leached. The 3D hollow spherical structure prevented aggregation of iron atoms, offered shorten pathway for mass diffusion and exposed more active sites.[61] Li et al. synthesized Fe–N–C catalysts that possess special atomically dispersed Fe-N_x structure via changing the ratio of acrylic acid (AA) and maleic acid (MA). AA could be polymerized into PAA and chelated with Fe^{3+} to form a cross-linked hydrogel, while MA could be co-polymerized with AA to increase the carboxylic content of the copolymer (P(AA-MA)). These polymers and cyanamide were treated at high-temperature to obtain PAA–Fe–N and P(AA-MA)–Fe–N. Structural characterization results showed that the introduce of MA elongate the bond strength of Fe–N and create the exclusive Fe–N_4/C moiety of P(AA-MA)-Fe-N.[62]

Generally, high temperature pyrolysis is the most mature method for preparing Fe_{SA}–N–C. By adjusting the size, coordination number and composition of the MOF precursor, a more precise tuning of the catalyst can be achieved. In addition, pyrolysis of irregular metal-containing complexes and polymers enable more structurally diverse Fe_{SA}–N–C catalysts with more abundant iron sources, carbon sources and nitrogen sources. Remarkably, during the process of high temperature pyrolysis,

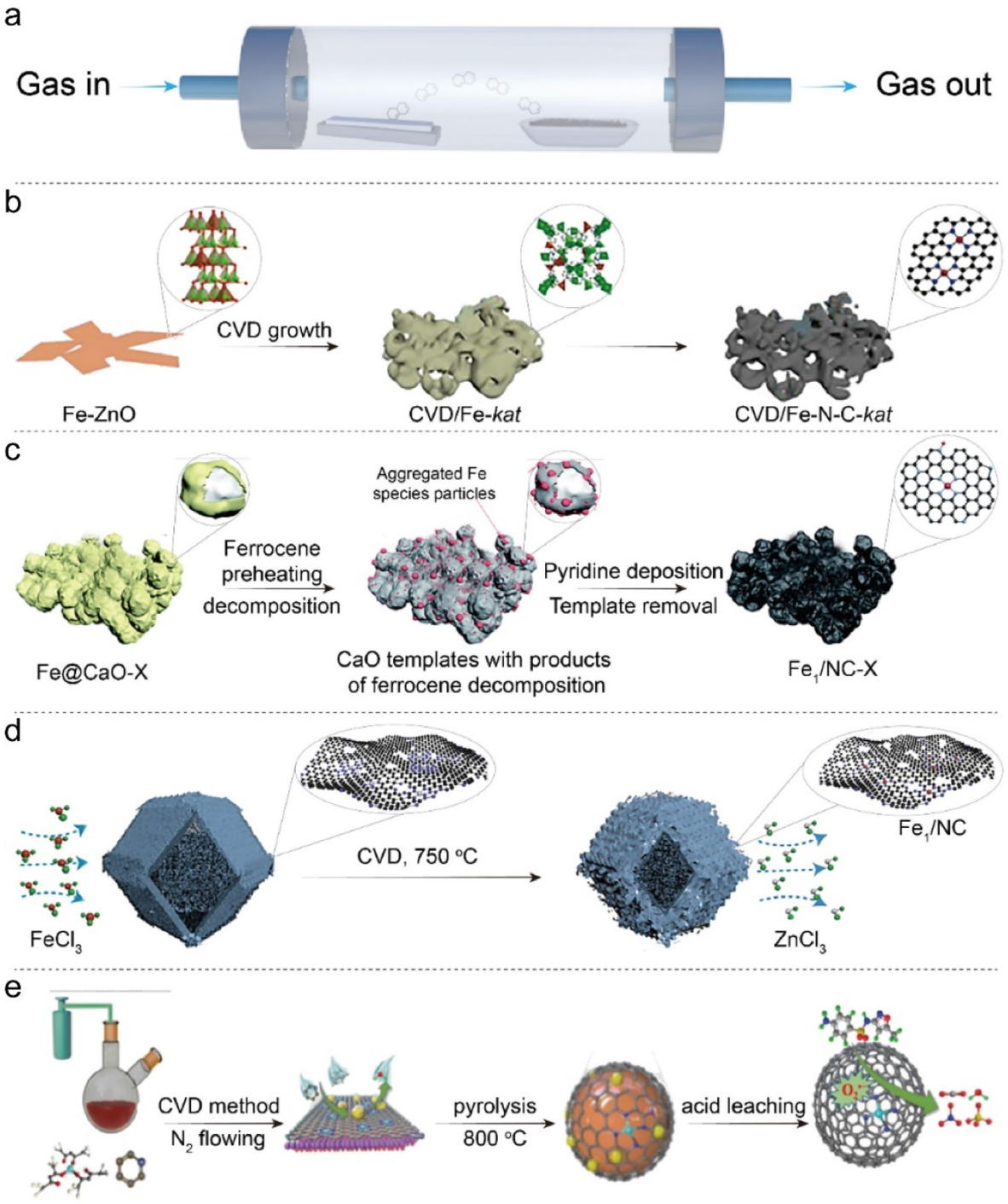

Fig. 3. Schematic illustration of (a) CVD method, (b) one-pot synthesis process of atomically dispersed Fe–N–C catalysts via a CVD method, (c) synthesis of SAMs with Fe-atoms anchored on 3D N-doped carbon nanosheets and the corresponding Fe–N_4 coordination structure, (d) synthesis of FeNC-CVD-750 via $FeCl_3$ CVD, (e) synthesis of Fe–N–PC materials. Reproduced with permission from (a, b) Ref. 63, (c) Ref. 66, (d) Ref. 67, (e) Ref. 64.

the introduction of template can further regulate the microstructure and pore size of the Fe_{SA}–N–C catalysts, thus improving their catalytic performance and stability.

2.2. Chemical vapor deposition (CVD) method

Due to low metal loading in high temperature pyrolysis methods, the chemical vapor deposition (CVD) method was designed to synthesize Fe–N–C catalysts (Fig. 3a).[63–67] One of the most important advantages of the CVD method is the ability to select different templates and adjust deposition conditions to precisely control the morphology and pore structure of the resulting catalysts.[68]

Wu et al. prepared atomically dispersed Fe–N–C catalyst with increased Fe loading via CVD method compared to wet-chemistry synthesis. As shown in Fig. 3b, with the presence of argon gas and heating, gaseous 2-MeIm was deposited onto Fe–ZnO nanosheets and underwent a gas-solid reaction to form Fe–$Zn(MeIm)_2$ intermediate and its crystalline structure gradually evolved from *zif* towards *kat* phase. The formation of CVD/Fe-*kat* increased the number of active sites, which was attributed to the fact that the formed narrower pores could promote the coordination of single Fe sites with N and thus slow down the diffusion and agglomeration of Fe atoms. Finally, CVD/Fe–N–C-*kat* was obtained under 1000 °C heating. According to the analysis of in-situ electrochemical measurements through the nitrite absorption followed by reductive stripping, the FeN_4 active site density of CVD/Fe–N–C-*kat* is about 26 mmol g^{-1}, which is higher than most Fe–N–C catalysts synthesized by other methods.[63] Similarly, Peng et al. chose ferrocene-doped calcium oxide as a template and pyridine as carbon and nitrogen sources to synthesize atomic Fe–N–C catalyst by pyrolysis at 700 °C under an argon atmosphere via CVD method (Fig. 3c).[66] Later, they used iron(III) acetylacetonate dissolved in pyridine as a precursor, magnesium hydroxide as a substrate for CVD pyrolysis, and finally acid etching to obtain single iron atoms anchored on porous N-doped carbon (Fe-N-PC) (Fig. 3e).[64]

Jia and co-workers creatively synthesized Fe–N–C with high active sites by flowing ferric chloride vapor over Zn–N–C at 750 °C via CVD method (Fig. 3d). Zn–N–C material was obtained by pyrolysis of ZIF-8 under argon atmosphere at 1050 °C, which contained 2.16% Zn and abundant microporous structures. In the presence of $FeCl_3$, the Zn was removed and Fe took the place of Zn under high temperature (>650 °C), which contributed to the formation of Fe–N_4 sites according to the reaction mechanism: $FeCl_3(g) + Zn–N_4 + X \rightarrow Fe–N_4 + ZnCl_2(g) + XCl$ (X refers to H or Cl). The obtained FeNC-CVD-750 catalyst had an activity site density of 1.92×10^{20} sites per gram with 100% site utilization.[67] In short, although the CVD method can appropriately increase the loading of iron atoms, its complex synthesis steps and high temperature condition force a preference for simpler methods to synthesize single-atom catalysts.

2.3. Ball milling method

Traditional ball milling method involves mixing metal salts, nitrogen-containing compounds and supports by ball milling and then thermal reducing the mixture to form single atom catalysts. The purpose of ball milling is to improve metal dispersion before pyrolysis. Dai et al. reported a universal domino reaction strategy to produce M-SA/NC catalysts including Fe, Co, Ni, Mn, Mo, Pd and arbitrary combinations SA/NC catalysts (Fig. 4a). Polyaniline (PANI), appropriate metal salt, NaCl and $NaNO_3$ were mixed and ball-milled with the aim of making PANI chains doped with metal ions and wrapped around salt particles. $NaNO_3$ was decomposed and released gases to cause PANI blew up and carbonized with the formation of porous carbon nanosheets by pyrolysis at 1000 °C. The role of the gas is to etch the nanosheets for obtaining a microporous structure and also to anchor the metal atoms to the carbon framework and prevent them from aggregating into metal particles. In addition, the structure and pore size of M-SA/NC could be regulated by changing the content of $NaNO_3$.[69]

The other means of synthesis is to directly high-energy ball milling coordination precursors (such as iron phthalocyanine) and carbon supports to achieve mixing in molecular-level and provide precursors for the subsequent pyrolysis.[70,71] Deng et al. used the ball milling approach to synthesize a highly dispersed single FeN_4 center with coordinatively unsaturated iron sites confined in a graphene matrix at a large quantity with iron phthalocyanine (FePc) and graphene nanosheets as precursors (Fig. 4b).[70] During the ball milling process, on one side, the outside macrocyclic structure of FePc is disrupted to produce a fragmented structure possessing FeN_4. On the other side, graphene produces

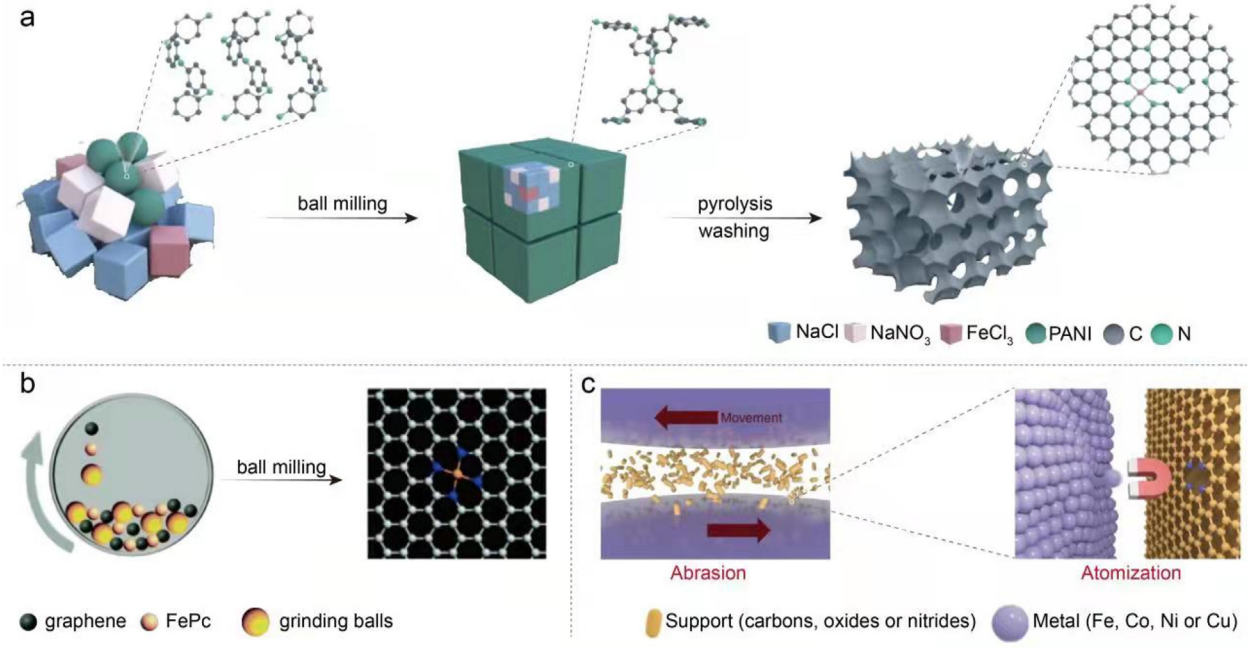

Fig. 4. Schematic illustration of (a) synthesis of M-SA/NC via ball milling, (b) ball milling approach to graphene-supported FeN4, (c) mechanism for forming a SAC via abrasion method. Reproduced with permission from (a) Ref. 69, (b) Ref. 40, (c) Ref. 32.

defective sites and interacts with isolated FeN_4 centers.

Under the influence of the above two ball milling methods, Baek et al. discovered an eco-friendly top-down strategy, namely mechanochemical abrasion method, which means the direct atomization of bulk metals on different supports by means of abrasion, without any solvent and the generation of by-products and waste in the process (Fig. 4c).[32] In the experiment, iron balls, N_2 gas and graphite were loaded into a steel container and the ball-milling was conducted at a constant rotation speed for 30 h. Iron balls are not only the source of iron single atoms, but also transfer kinetic energy to drive reactions. N_2 gas is dissociated on the surface of the iron balls and enters the graphite framework to anchor the iron atoms. The graphite is served as an active matrix to accommodate the nitrogen and atomized metal. An additional advantage of the abrasion method is that the amount of catalyst can be expanded in equal proportions by increasing the volume of the ball-milling container.

In general, Table 1 lists the advantages and disadvantages of these three preparation methods for Fe–N–C single atom catalysts. Compared to other synthesis methods, ball milling method simplifies the synthesis process and is prone to be applicable for the large-scale preparation of Fe–N–C. However, during the ball milling process, some of iron atoms may be encapsulated inside the catalysts, which in turn results in a low atomic utilization and uneven structures.

3. Property

There are many factors affecting the properties of Fe–N–C electrocatalysts, such as the electronic structure of the central metal, the metal coordination environment, and the metal-support interactions. But little attention has been paid to the role of electron spin of Fe. As the following, we will discuss spin-related properties in Fe–N–C catalysts.

3.1. Fe–N–C electron structure and spin

In general, FeN_x moieties serve as active sites of most Fe–N–C catalysts, while the number of coordination x usually depends on the synthesis conditions. The coordination environment and the valence state of iron determine the spin state of single Fe atom. Fig. 5 shows the electronic configuration and spin state of the common FeN_4 species. When oxidation state of Fe is +1 or +4, the 3d electron configuration of FeN_4 is $d_{xy}2d_{yz}2d_{xz}2d_{z^2}1$ or $d_{xy}2d_{yz}1d_{xz}1$, respectively, belonging to low spin states. When oxidation state of Fe is +2, the 3d electron configuration of Fe(II)N_4 can simply be classified into three forms, including $d_{xy}2d_{yz}2d_{xz}2$, $d_{xy}2d_{yz}2d_{xz}1d_{z^2}1$ and $d_{xy}2d_{yz}1d_{xz}1d_{z^2}1d_{x^2-y^2}1$, corresponding to low spin $t_{2g}6e_g0$, medium spin $t_{2g}5e_g1$ and high spin $t_{2g}4e_g2$, respectively. When oxidation state of Fe is +3, the 3d electron configuration of Fe(III)N_4 can simply be classified into three forms, including $d_{xy}2d_{yz}2d_{xz}1$, $d_{xy}2d_{yz}1d_{xz}1d_{z^2}1$ and $d_{xy}1d_{yz}1d_{xz}1d_{z^2}1d_{x^2-y^2}1$, corresponding to low spin $t_{2g}5e_g0$, medium spin $t_{2g}4e_g1$ and high spin $t_{2g}3e_g2$, respectively. Most of the reports demonstrate that the preparation method and preparation conditions have important effects on the spin of iron in Fe–N–C catalysts, including the type and content of iron, pyrolysis temperature, pyrolysis duration, atmosphere, etc. Additionally, it must be mentioned that heteroatom doping and the modulation of supports could also change the iron electron polarization as well as the electron spin state and complete mutual transformation of different spin states.

Table 1
The advantages and disadvantages of high temperature pyrolysis, chemical vapor deposition (CVD) and ball milling method.

Method	Advantages	Disadvantages
High temperature pyrolysis	A more homogeneous structure; Abundant sources of carbon and nitrogen	Low loading amount; Not suitable for large-scale preparation
Chemical vapor deposition (CVD)	High site densities; Controllable morphology; Controllable loading amount	Complex preparation process; Requires high temperatures.
Ball milling	Simple synthesis steps; Large-scale preparation; Without the use of solvents	Uneven Structure; Low iron atoms utilization rate

Commonly used detection tools for measuring the spin state of Fe include electron paramagnetic resonance (EPR), L-edge X-ray absorption near edge structure (XANES) and Mössbauer spectroscopy. When there are unpaired electrons in the outer electron orbitals of iron, under an applied magnetic field and an applied electromagnetic wave, the electrons at the low spin energy level absorb energy and transfer to the high spin energy level to produce paramagnetic resonance absorption, which is the reason why EPR can measure the spin state of iron. However, there is a serious limitation of EPR that it can only provide information on iron with half-integer spin multiplicity and cannot measure the valence state of all iron species. Fe L-edge XANES is employed to analysis the structure of Fe, because the valence and spin states of 3d tradition metals significantly affect the L-edge spectra. The L-edge of 3d tradition metals is generated by electronic transitions between the 2p level and the mostly unoccupied 3d electronic states. The L_3 edge (706–712 eV) involves transitions from $2p_{3/2}$ to 3d states, while the L_2 edge (718–726 eV) comes from transition $2p_{1/2}$ to 3d states. Additionally, it has been found that there is a relationship between the area ratio of L_3/L_2 and the spin state. A higher ratio indicates that high spins dominate, and vice versa.[72–74] However, the sensitivity of XANES to the spin state of the fine structure containing iron is not as good as that of the Mössbauer spectrum.

The ^{57}Fe Mössbauer spectroscopy, involving the resonant and recoil-free emission and absorption of γ-rays by atomic nuclei, is used to study the valence, spin polarization and coordination environment of iron in single-atom catalysts based on the values of isomer shift (IS) and quadrupole splitting (QS).[74–76] Each type of iron with a defined coordination structure and spin state corresponds to a specific value of IS and QS, and the shift of values implies the change of iron species. In addition, with the development of operando spectroscopy, operando Mössbauer spectroscopy could be used to characterize the spin state of iron-based materials during reactions. As a result, the Mössbauer spectrum has become the most reliable means to characterize the spin state of iron-based materials.

Recently, non-resonant X-ray emission spectroscopy (XES) was demonstrated to quantify the average, ex situ spin state of a series of Fe–N–C catalysts. Herranz et al. used two-component fitting to analyze the K_β main lines based on a linear relation between the relative area of the $K_{\beta'}$ spectral peak and the spin state of several reference compounds, and in turn established a potential-induced spin change in the catalysts prepared by pyrolysis of an Fe-porphyrin.[77] Excitingly, this method has the potential to be extended to measure the spin state of other transition metal materials. However, it always reflects an average spin state information and cannot help us to determine the influence of the spin state on the reaction mechanism at a deeper level.

3.2. Coupling between electronic structure of Fe–N–C and electronic (orbit) of C, N, O

Numerous experimental evidences show that the spin of Fe affects the occurrence of the reaction as well as the rate and selectivity of the reaction. Next, we will further analyze the effect of spin on the reduction of C, N and O from the perspective of orbital coupling.

The activation of CO_2 plays an important role in the process of $CO_2 \rightarrow CO$. The HOMO of CO_2 localize on the O atom, while the LUMO localize on the C atom and performed as a C–O σ* orbital. Taking Fe(I) L.S. as an example, the electron-rich iron center conducts nucleophilic attacks on the electrophilic C-center of CO_2, which means that occupied d_{z^2}, d_{yz} and d_{xz} orbitals of iron could offer electrons to populate these empty σ* and π* orbitals, which is beneficial to the activation of CO_2 (Fig. 6a, d). When CO_2 gets an electron, a new splitting of the CO_2 orbitals occurs, but the coupling tendency with Fe will not change greatly.[78]

Taking Fe(III) M.S. as an example, the iron centers have empty $d_{x^2-y^2}$ orbitals and the half-filled d_{z^2} orbitals (Fig. 6b). Upon the N_2 side-on

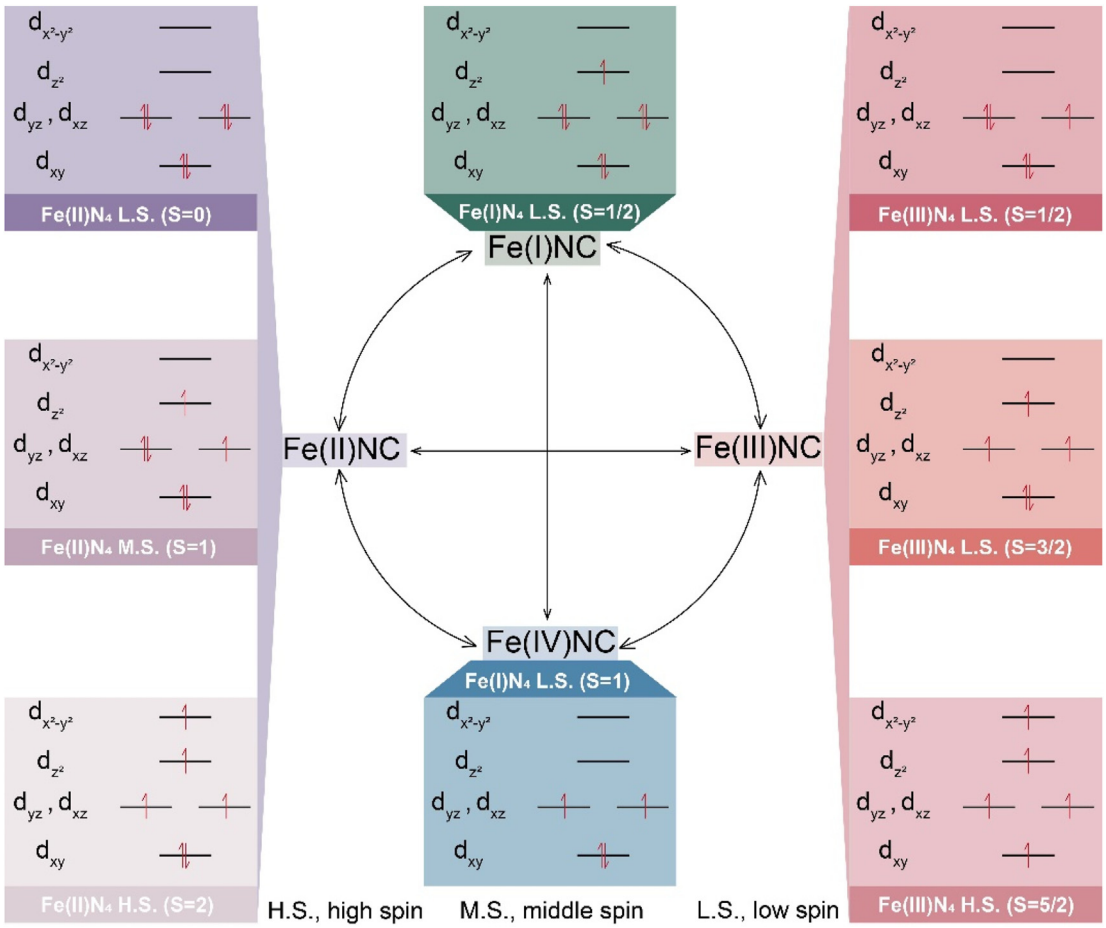

Fig. 5. 3d electronic structure of FeN_4 species with different oxidation states and common spin states of iron and their transformation into each other (L.S., M.S. and H.S. corresponds to low spin, middle spin and high spin, respectively and S refers to spin angular momentum.).

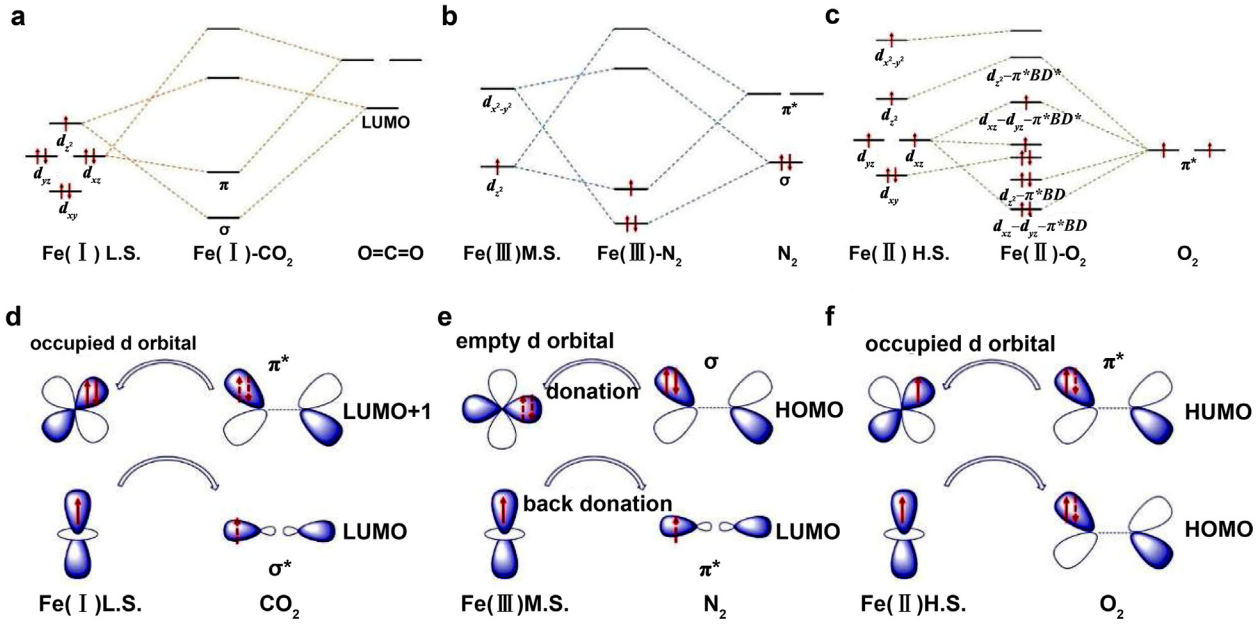

Fig. 6. Simplified schematic of bonding and coupling between (a, d) Fe(I) L.S. and CO_2, (b, e) Fe(III) M.S. and N_2 and (c, f) Fe(II) H.S. and O_2 to illustrate the symmetric matching rule and electron transition from the LUMO and HOMO.

adsorption, N_2-σ electrons will be transferred to higher-energy empty spin-down d-orbitals ($d_{x^2-y^2}$). The empty spin-down orbitals (d_{z^2}) at the higher energy interact with the antibonding orbitals of N_2 to weaken the N–N triple bond and lower the N_2 adsorption energy (Fig. 6e), which can explain why Fe(III) has excellent NRR performance.[79] The low spin Fe(II)N_4 lack of unpaired d electrons and the high spin Fe(II)N_4 lack of empty d orbitals showed poorly activity of N_2 reduction reaction. Similarly, the high spin Fe(III)N_4 exhibits worse activity than middle spin Fe(III)N_4 and low spin Fe(III)N_4 due to the shortage of empty d orbitals.[80]

Fig. 6c illustrates the major orbital interactions between O_2 and high spin Fe(II) during the O_2 adsorption process. The antibonding orbital (π*) of O_2 could couple with the half-filled d_{z^2}, d_{yz} and d_{xz} orbitals to form four new low-to-high orbitals, corresponding to $d_{xz}-d_{yz}-\pi^*BD$, $d_{z^2}-\pi^*BD$, $d_{xz}-d_{yz}-\pi^*BD^*$ and $d_{z^2}-\pi^*BD^*$, which increases the d orbital splitting and form a more stable system (LS Fe(II)-O_2). From the electronic point of view, it can be roughly considered that the d electrons of d_{z^2}, d_{yz} and d_{xz} orbitals leap to the π* orbital of O_2, resulting in electrons rearrangement that occur to reduce the energy of the system (Fig. 6f). It is also worth mentioning that the interaction between iron species and O_2 should not be too strong. Low spin Fe(III) without e_g filling has empty σ* antibonding orbital of FeN_4, and leads to a very strong Fe(III)/O_2 interaction and a quite stable Fe^{4+}–O_2^{2-} bond. Thus, it is difficult for the occurrence of Fe(IV)-O_2/Fe(III)-OOH transition.[81,82]

4. Application

4.1. Reduction of carbon

4.1.1. Carbon dioxide reduction reaction (CO_2RR)

Electrocatalytic carbon dioxide reduction reaction is a significant strategy to solve the problem of energy shortage and environmental pollution. Carbon dioxide could be reduced to value-added chemical products powered by electricity generated from renewable energy sources.[83] Many studies have shown that Fe–N–C exhibits remarkable performance concerning the reduction of CO_2 to CO and other simple chemicals (Table 2).

Hu et al. reported Fe–N–C catalyst with atomically dispersed iron sites, which produced CO at the overpotential of −0.08 V in the CO_2-saturated 0.5 M $KHCO_3$ catholyte. When the cathode potential decreased to −0.45 V (vs. RHE), particle current density of CO could reach 94 mA cm^{-2} with FE_{CO} higher than 90%. Fe $2p_{3/2}$ XPS spectrum and Fe K-edge XANES spectrum results indicated that the iron oxidation state of Fe–N–C was +3. Compared to Fe–N–C, the current density of Zn–N–C synthesized under the same conditions could be neglected at −0.1 V to −0.6 V (vs. RHE), indicating that Fe sites was the origin of Fe^{3+}–N–C during CO_2RR. Operando XANES displayed that the Fe K-edge of Fe^{3+}–N–C showed no obvious shift at −0.1 V to −0.4 V (vs. RHE), indicating the Fe species remained in +3 oxidation state; while Fe K-edge shifted to lower energies at −0.4 V to −0.5 V (vs. RHE), the same as the potential of the deactivation of Fe^{3+}–N–C, indicating the reduction of Fe^{3+} to Fe^{2+} (Fig. 7a). Furthermore, it could be observed that Fe^{3+} was reduced to Fe^{2+} in the as-prepared Fe^{3+}–N–C at −0.1 V to −0.2 V (vs. RHE) (Fig. 7b). These phenomena proved that Fe^{3+} sites were more active for generating CO. According to the kinetic and mechanistic analysis (Fig. 7e), CO_2 adsorption is the rate-limiting-step for Fe^{2+}–N–C, while the protonation of the adsorbed CO_2^- to form an adsorbed COOH intermediate is the rate-limiting-step for Fe^{3+}–N–C. Additionally, the CO_2RR rate would be also limited by CO desorption for Fe^{2+}–N–C but not limited for Fe^{3+}–N–C. As a result, the superior activity of Fe^{3+} could be proven to derive from faster CO_2 adsorption and weaker CO adsorption compared to Fe^{2+} sites.[84] Liu et al. identified low-spin Fe(I)N_4 is the reactive center for the conversion of CO_2 to CO. Operando ^{57}Fe Mössbauer results showed that three doublets were detected in the Fe–NC–S at OCV, corresponding to LS Fe(II)N_4, MS Fe(II)N_4 and HS Fe(II)N_4, respectively. When polarized at −0.3 V (vs. RHE), a new doublet was observed and was assigned to LS Fe(I)N_4. When the potential was gradually decreased to −0.9 V (vs. RHE), the relative content of LS Fe(I)N_4 increased accompanied by the decreasing of relative content of LS Fe(II)N_4, which reflected that LS Fe(II)N_4 was reduced to LS Fe(I)N_4. Additionally, the new doublet disappeared when removing the potential, further proving that Fe(I)N_4 transited from LS Fe(II)N_4 was the real active center during CO_2RR (Fig. 7c). DFT calculations indicated that the CO_2 molecule is activated on the Fe(I) site and then forms the *COOH intermediate after the hydrogenation step. During the process, the singly occupied d_{z^2} orbital of Fe(I) coupled with the singly occupied π_1* orbital of COOH to generate one fully occupied bonding ($d_{z^2}-\pi_1^*BD$) orbital and one empty antibonding ($d_{z^2}-\pi_1^*BD^*$) orbital (Fig. 7d). Next, *CO and H_2O are generated in the presence of electrons and protons. Finally, the adsorbed CO desorbs from the Fe(I) site to complete the catalytic cycle.[75]

To further understand the effect of spin state of single-atom FeN_4, Chen et al. conducted a more detailed analysis on the electroreduction of CO_2 to CO/HCOOH. Combined with the Fe^{2+} radius, energy order and corresponding HOMO–LUMO gap of calculated Fe(II)N_4 in the different spin states, the order of catalyzing activity is inferred to Fe(II)N_4(MS) > Fe(II)N_4(LS) > Fe(II)N_4(HS). Moreover, the calculation of CO_2 absorption energy indicated the adsorption strength decreases with the increase of the spin states for Fe(II)N_4. Furthermore, it is clear that the middle spin Fe(II)N_4 has the lowest energy barrier for the first-step reduction of CO_2 (0.52 eV) compared to other two spin states. As a result, the middle spin Fe(II)N_4 have the highest selectivity and best activity from the perspective of mechanism. The same approach proves that the middle spin Fe(III)N_4C favors the conversion process of *CO_2 to *COOH as compared with the other two spin states.[89]

Table 2
Summary of recently reported representative Fe–N–C-based catalysts for CO_2RR.

Catalyst	Electrolyte	Product	Faradaic efficiency (vs. RHE)	Current density (mA cm^{-2})	Reference
Fe^{3+}–N–C	0.5 M $KHCO_3$	CO	>90% @ −0.45 V	94	[84]
Fe–NC–S	0.5 M $KHCO_3$	CO	93% @ −0.4 V	4	[75]
Fe_1–NSC	0.5 M $KHCO_3$	CO	98.6% @ −0.48 V	–	[85]
Fe–FN–C	0.5 M $KHCO_3$	CO	90.4% @ −0.5 V	2.68	[86]
Fe–N/P–C	0.5 M $KHCO_3$	CO	98% @ −0.45 V	–	[87]
FeN_4Cl/NC	0.5 M $KHCO_3$	CO	90.5% @ −0.6 V	9.78	[88]

4.2. Reduction of nitrogen

4.2.1. Nitrogen reduction reaction (NRR)

The industrial production of ammonia is mainly dependent on the Haber–Bosch process under harsh conditions, which accounts for 1%–2% of the earth's energy supply.[97,98] Moreover, this process can only obtain relatively low conversions due to the constraints of chemical equilibrium. Therefore, it is of great significance to develop efficient nitrogen fixation routes under mild conditions. Inspired by the fact that bacteria can electrochemically reduce nitrogen in the presence of enzyme nitrogenase, electrochemical N_2 reduction reaction via $N_2(g)+6H^++6e^-\rightarrow 2NH_3(g)$ received a lot of attention.[99] Unfortunately, hydrogen evolution reaction (HER) is more likely to occur at similar potentials at most of the metal active sites due to the yield of a large amount of electrons and protons. From the kinetic point of view, the activation of N_2 is the rate determining step of nitrogen reduction reaction.[100] Fe–N–C is thought to be ideal electrocatalysts for lowering the free barrier of N_2, weakening hydrogen absorption, and improving ammonia selectivity due to the dispersion of active sites and the positive charge of the metal (Table 3).[101]

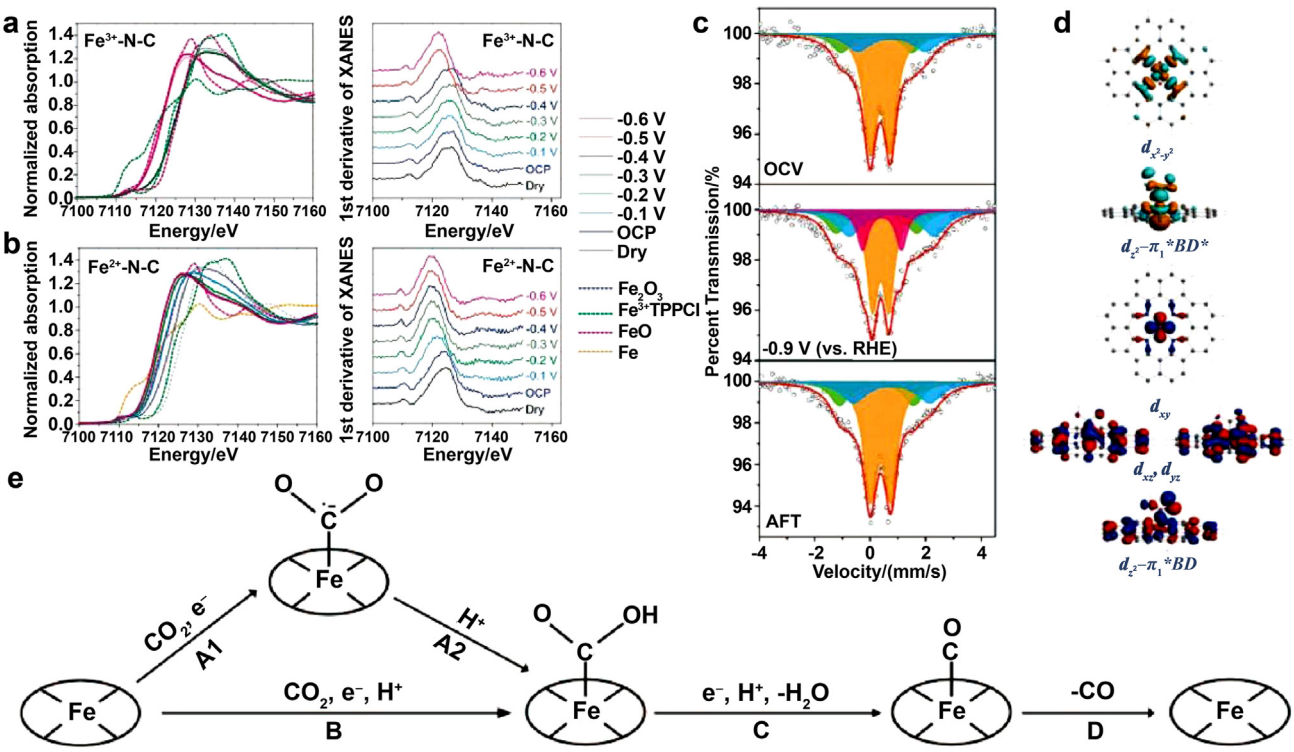

Fig. 7. Operando XAS characterization of (a) Fe^{3+}–N–C and (b) Fe^{2+}–N–C, excluding Fe k-edge XANES spectra and first derivative of the spectra at different potentials. (c) Operando ^{57}Fe Mössbauer spectra of ^{57}Fe-enriched Fe–NC–S at open-circuit voltage (OCV), −0.9 V (vs. RHE) and after CRR (AFT) in CO_2-saturated 0.5 M $KHCO_3$ solution. (d) Selected contour plots of molecular orbitals for the *COOH intermediate with the LS Fe(I)N_4. (e) Proposed reaction pathways of CO_2 electroreduction to CO. Reproduced with permission from (a, b) Ref. 84, (c, d) Ref. 75, (e) Ref. 84.

Table 3
Summary of recently reported representative Fe–N–C-based catalysts for NRR and NitRR.

Catalyst	Reaction	Electrolyte	Faradaic efficiency (vs. RHE)	Yield rate/μg h^{-1} $mg^{-1}_{cat.}$	Reference
Fe–N/N–CNTs	NRR	0.1 M KOH	9.28% @ −0.2 V	34.83	90
ISAS–Fe/NC	NRR	0.1 M PBS	18.6% @ −0.4 V	62.9	91
FePc/C	NRR	0.1 M Na_2SO_4	10.5% @ −0.3 V	137.95	92
Fe_{SA}–NC	NRR	0.1 M KOH	56.55% @ 0 V	7.48	46
Fe–N–C	NitRR	0.5 M KNO_3/0.1 M K_2SO_4	75% @ −0.66 V	~20000	93
Fe–PPy SACs	NitRR	0.1 M KNO_3/0.1 M KOH	100% @ −0.7 V	2750	94
Fe–CNS	NitRR	$NaNO_3$/Na_2SO_4	78% @ −0.57 V	~26800	95
FeMo–NC	NitRR	0.05 M PBS/0.16 M KNO_3	94% @ −0.45 V	153	96

Thanks to high stability and high carrier mobility, graphene is expected to facilitate charge transfer in catalytic reactions. As early as 2016, Luo et al. proposed a new catalyst, FeN_3-embedded graphene, for activating N_2 and converting it into NH_3 at room temperature from first-principles calculations. From the perspective of chemical coordination, the FeN_3 center is strongly spin-polarized with a localized magnetic moment, which greatly facilitates the adsorption of N_2 and activates the inert N≡N bond. The synergistic interaction between graphene and FeN_3 gives the system novel properties to catalyze the conversion of activated N_2 to NH_3 via a six-proton and six-electron process at room temperature following three possible reaction paths.[102] On this basis, Zheng et al. designed and synthesized Fe–N/N–CNTs with built-in Fe–N_3 sites by pyrolysis of Fe-doped ZIF–CNTs templates. The NRR performance indicated that Fe–N/N–CNTs possessed the highest NH_3 average yield of 34.83 μg h^{-1} $mg^{-1}_{cat.}$, and corresponding FE of 9.28% at −0.2 V (vs. RHE).[90]

Later, more and more studies have found Fe–N_4 structure possess higher intrinsic activity and obvious ability to inhibit hydrogen evolution. Liu et al. reported a Fe single-atom catalyst with well-defined Fe–N_4 active sites and in neutral media, achieving high Faradaic efficiency (18.6 ± 0.8%) and NH_3 yield rate (62.9 ± 2.7 μg h^{-1} $mg^{-1}_{cat.}$) at −0.4 V (vs. RHE) at room temperature.[91] Hu et al. developed a method to prepare iron-nitrogen-carbon materials for electrocatalysis N_2 reduction reaction by loading iron phthalocyanine (FePc) on nano/microporous carbon at a molecular level. It delivered a high selectivity and activity with a NH_3 yield rate of 137.95 μg h^{-1} mg^{-1}_{FePc} at the potential of −0.3 V (vs. RHE) in 0.1 M Na_2SO_4 aqueous solution. On the basis of systematic electrochemical analyses, poisoning experiments and theoretical calculations, it suggested that Fe center in FeN_4 was the most active site for NRR rather than N or C sites.[92] Yan et al. demonstrated a single atomic iron catalyst on nitrogen-doped carbon (Fe_{SA}–N–C), which promoted NRR process with a Faradaic efficiency of 56.55% at an onset potential of 0.193 V and a desirable ammonia yield rate of 7.48 μg h^{-1} mg^{-1} at 0 V in alkaline solution. Molecular dynamics simulation unveiled that N_2 molecules tended to accumulate at approximately 0.45 nm from the Fe site, leading to high local concentrations, which would promote the following adsorption (Fig. 8a). DFT calculations proved that the energy barrier of N_2 absorption is much lower than that of water dissociation (Fig. 8b) and the alternating pathway was prone to achieve NRR (Fig. 8c). These results illustrated that Fe_{SA}–N–C was more favorable for nitrogen adsorption than hydrogen adsorption with a small energy barrier.[46]

In order to understand the relationship between the electronic state of

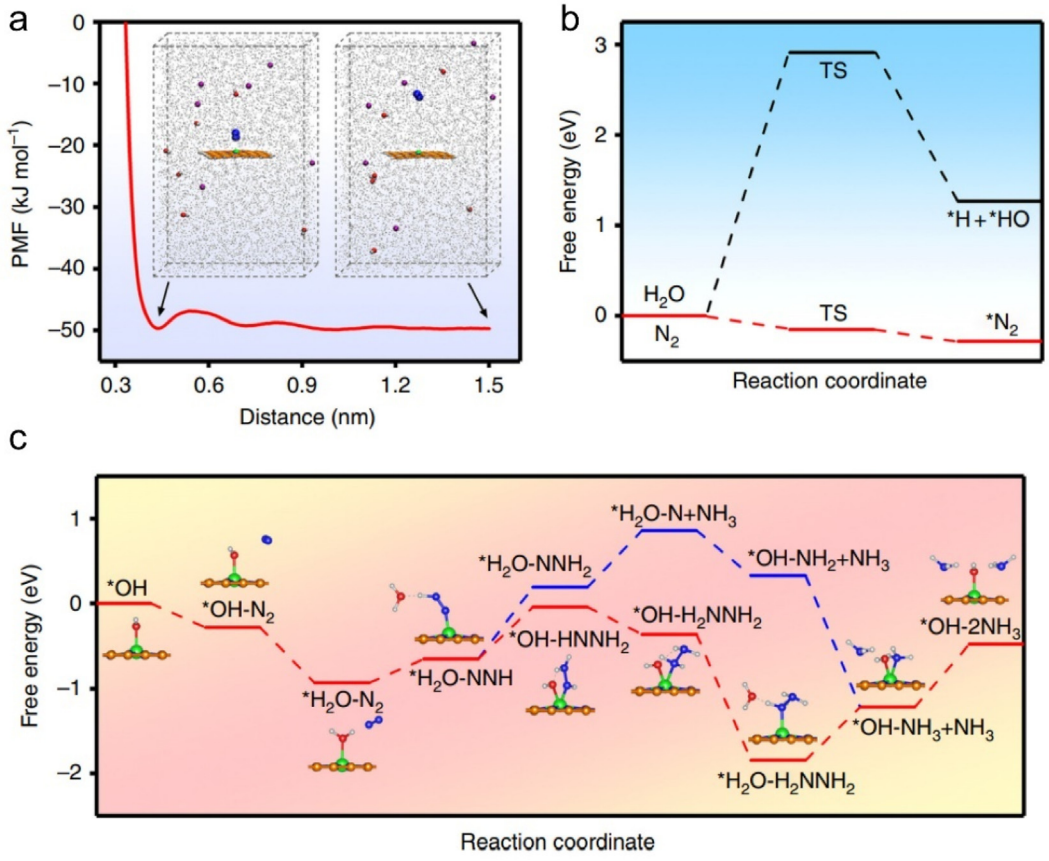

Fig. 8. (a) Potential of the mean force for N_2 adsorption on the Fe_{SA}–N–C in 0.1 M KOH, inset: molecular dynamics simulation snapshots at 0.45 and 1.5 nm. (b) Calculated energy barriers of the adsorption of hydrogen and nitrogen. (c) Free energy diagram for the NRR on the Fe_{SA}–N–C catalyst at $U = 0$ V.[46] Reproduced with permission from Ref. 46.

FeN_4 and NRR, Zhang et al. fabricated Fe and Mo co-coordinated polyphthalocyanine electrocatalyst (FeMoPPc) by a low-temperature melt polyphthalocyanine. The zero-field cooling temperature-dependent magnetic susceptibility measurements and ^{57}Fe Mössbauer spectra revealed that Fe(II) changed from high spin to middle spin after adding Mo, which weakened the N≡N bond and promoted the first hydrogenation of N_2.[80] In addition, Feng et al. found that F surface modification could induce Fe(III) in the high spin state, which facilitated π-back-donation process, promoted the activation of N_2 and reduced the limiting potential of NRR.[103]

4.2.2. *Nitrate reduction reaction (NitRR)*

The misuse of nitrogen fertilizers and the consumption of fossil fuels have made nitrate ions one of the most spread water contaminants, posing a serious threat to the ecology and human health.[104,105] Nitrate reduction reaction converts NO_3^- to N_2 or NH_3 under a wild temperature and pressure, playing a vital role in promoting the earth's nitrogen cycle and solving water pollution problems. In recent years, a series of metal catalysts have been used to convert nitrate to nitrogen, including Ru, Rh, Ir and Cu.[106,107] However, there have been few studies on the reduction of nitrate wastes to value-added ammonia. As a vital competition, NO_3^- reduction to N_2 involves an N–N coupling step, which needs two neighboring active sites. Therefore, selecting suitable single atom catalyst can improve the selectivity towards ammonia. So far, Fe–N–C was reported to perform excellent activity of NitRR, which could help us understand the complex pathways and mechanism of the 8 protons and 8 electrons transfer process (Table 3).[93–95]

Wang et al. synthesized a single atomic Fe–N–C catalyst by a TM-assisted carbonization method with highly mesoporous structures. At a potential of −0.66 V (vs. RHE), Faradaic efficiency of the ammonia increased to a maximal of ~75%. A large NH_3 partial current density of ~100 mA cm^{-2} and a yield rate of ~20,000 μg h^{-1} mg cat^{-1} (0.46 mmol h^{-1} cm^{-2}) were obtained at the potential of −0.85 V (vs. RHE). The catalyst still exhibited excellent stability with a high NH_3 yield rate and FE after 20 consecutive electrolysis cycles under the best NH_3 selectivity reaction condition. DFT calculations reveal the minimum energy pathway for NO_3^- reduction to NH_3 on Fe single atom site (Fig. 9a). Furthermore, Fig. 9b exhibited NO* is a key intermediate and a limiting potential of $U = -0.30$ V is needed to make all steps downhill in free energy. These results proved the high NH_3 yield rate and activity of Fe SAC contributed to intrinsic high-efficiency active Fe–N_4 centers that exhibiting lower thermodynamic barriers and optimized electrocatalytic conditions.[93]

Later, Yu et al. demonstrated a polymer-hydrogel strategy for preparing single atom Fe catalysts anchored on N-doped porous carbon (Fe-PPy SACs). When the cathode potential varied from −0.3 V to −0.7 V (vs. RHE), The catalyst displayed a maximum ammonia yield rate of 2.75 mg_{NH3} h^{-1} cm^{-2} with nearly 100% Faradaic efficiency. Besides, The Fe–PPy SACs delivered a twelve times higher turnover frequency than Fe nanoparticles. The NitRR mechanism illustrated that the single active Fe-N_x site experienced a nitrate-preoccupied transition center and efficiently eliminated the competing water adsorption.[94] Later, Liu et al. found that doping of S could significantly enhance the activity of NitRR.[95] The catalyst (Fe–CNS) has many folds and defects according to the electrochemical active surface areas and pore size distributions, which suggested that S-doping could create more defect sites and shift the previously balanced electrons, leading to well electrical conductivity. Compared with Fe–CN, Fe–CNS showed higher NH_4^+–FE at all potentials. Moreover, the potential of maximum NH_4^+–FE (78%) with Fe–CNS was −0.57 V, higher than that of Fe–CN (−0.67 V). DFT calculations reflected

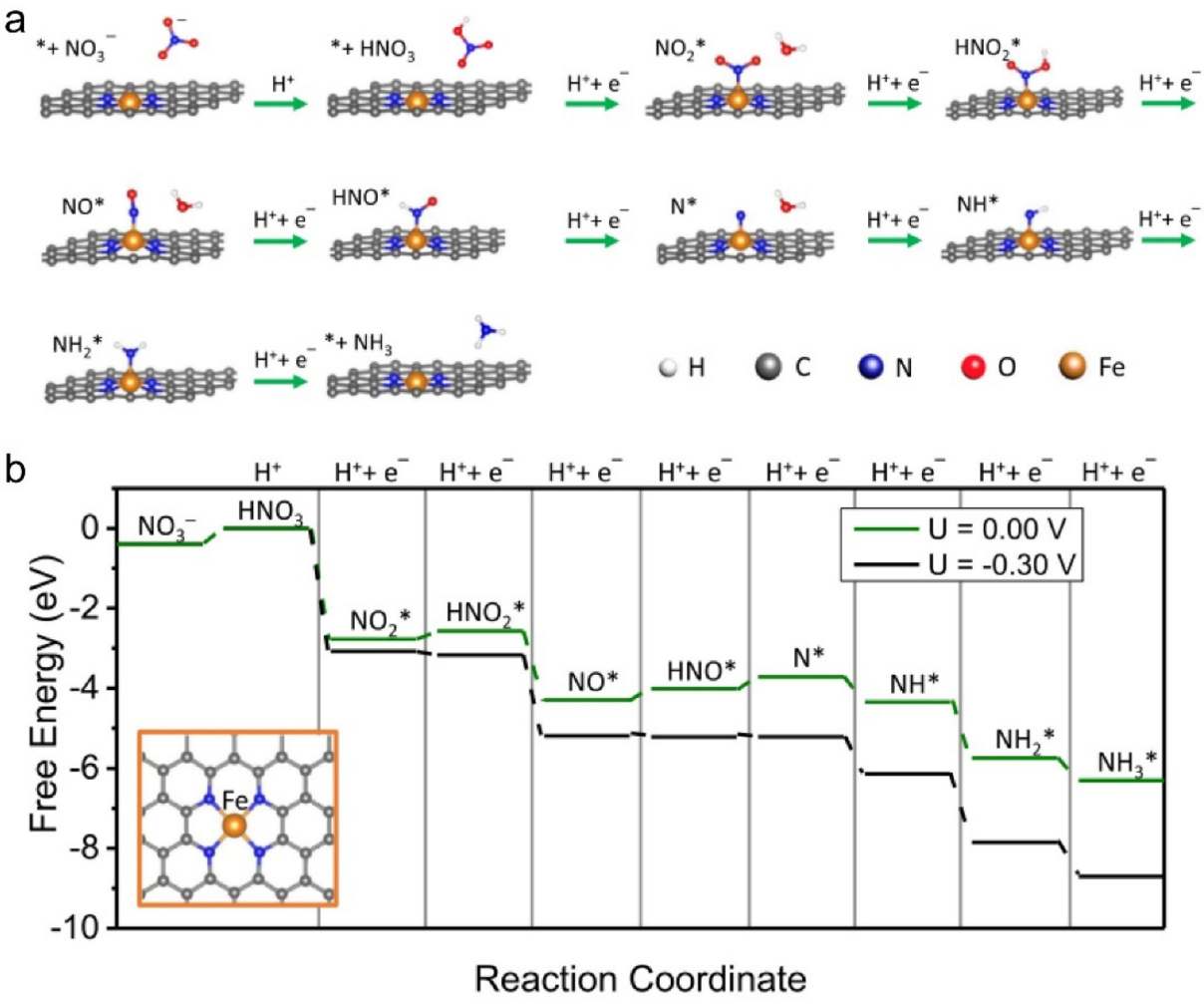

Fig. 9. (a) Minimum energy pathway that results in NH_3 as the main product. (b) Free energy diagram showing the minimum energy pathway at $U = 0.0$ V (vs. RHE) and at the calculated limiting potential of −0.30 V (vs. RHE).[93] Reproduced with permission from Ref. 93.

that the energy of the basic reaction ($NO_3^- \rightarrow NO_2^*$) changed from 2.02 eV to 2.37 eV after the doping of sulfur, which was consistent with the better catalytic performance of nitrate removal of Fe–CNS. And the energy changes for the basic reactions from N* to N_2* and from N* to NH* on Fe–CNS are −0.14 eV and 2.78 eV, respectively, which indicates that the ammonia path is thermodynamically favored. Unfortunately, no study has yet shown that the spin state of the iron center can affect the activity of nitrate reduction.

4.3. Reduction of oxygen

4.3.1. Oxygen reduction reaction($O_2 \rightarrow H_2O/OH^-$)

Proton exchange membrane fuel cells have broad application prospects due to their high efficiency and zero emission.[108] However, the slow cathodic reaction kinetics severely limits their development. Current electrocatalysts for this reaction are usually expensive, low storage capacity commercial Pt-based catalysts.[109] Therefore, it has become a top priority to search for efficient and stable ORR catalysts that could replace Pt. So far, among many single-atom transition metal catalysts, Fe–N–C with atomically dispersed iron sites has shown the best ORR catalytic performance (Table 4).[110,111] Oxygen reduction reactions are normally divided into a two-electron transfer process and a four-electron transfer process. The two-electron process reduces O_2 to hydrogen peroxide (H_2O_2), and the four-electron process directly reduces O_2 to H_2O under acidic conditions or hydroxide (OH^-) under alkaline conditions.[112,113] Hydrogen peroxide can react with iron sites in the Fenton reaction to produce reactive oxygen species, which in turn continuously leads to catalyst deactivation and degradation, and damage to the proton exchange membrane.[114] Therefore, we hope to further find Fe–N–C catalysts with high selectivity towards H_2O and well-defined mechanism.

Table 4
Summary of recently reported representative Fe–N–C-based catalysts for ORR.

Catalyst	Electrolyte	Half-wave potential/V (vs. RHE)	Onset potential/V (vs. RHE)	Reference
Fe–NC–S	0.1 M KOH	0.88	–	74
Fe_1–$NS_{1.3}C$	0.1 M KOH	0.86	0.97	115
Fe_1Se_1–NC	0.1 M KOH	0.88	1.0	116
FePc/$Ti_3C_2T_x$	0.1 M KOH	0.86	–	117
Fe–N–C/ N–OMC	0.1 M KOH	0.93	1.08	118
FeN_4–O–NCR	0.1 M KOH	0.942	1.05	119
Fe_{SAC}–MOF–5	0.5 M H_2SO_4	0.83	–	120
Fe–N–C/MA	0.5 M H_2SO_4	0.83	–	121
Fe,Mn/N–C	0.1 M KOH	0.928	–	122
	0.1 M $HClO_4$	0.804	–	

Xu et al. proposed a defined explain about the influence of local Fe(II) spin configuration on ORR. The higher spin state of iron in FeN_4 with bond contraction can create a wider spin-related channel in FeN_4, promoting the charge transport during ORR. Moreover, the oxygen molecule can be more easily captured by FeN_4 with Fe–N bond contraction because of higher bond order resulted from the spin–orbital interactions between

iron and O_2, which should be the intrinsic factor dominating the DFT calculated trend of O_2 adsorption.[117] Liu et al. firstly developed Operando ^{57}Fe Mössbauer to identify the exact structures and spin state of active atomically dispersed iron moieties during ORR. When polarized at 0.9 V (vs. RHE), it indicated that O_2 adsorbed on the HS Fe(II)N_4 sites along with the generation of O_2–Fe(II)N_5 intermediate and the spin state of Fe^{2+} transited from HS to LS with the central Fe^{2+} moving to the N_4-plane. When polarized at 0.7 V (vs. RHE), O_2 adsorbed on the LS Fe(II)N_4 sites along with the generation of O_2–Fe(II)N_4 intermediate and the spin state of Fe^{2+} transited from LS to HS with Fe^{2+} moving out of the N_4-plane (Fig. 10a and b). As shown in Fig. 10c, the spin crossover of Fe^{2+} significantly reduces the energy barrier for the dynamic cycle. Quantum chemical studies provide the structural and dynamic evolutions of Fe(II)N_4 and spin-crossover-involved mechanism for ORR (Fig. 10d). Due to the exchange stabilization, the interaction between O_2 and HS Fe^{2+} increases the d-orbital splitting, resulting in the conversion of the spin state of iron (Fig. 10e and f).[74]

Later, Zhai and co-workers reported that the incorporation of S in the second sphere of Fe–NC could enhance catalytic activity of oxygen electroreduction reaction via inducing the transition of spin polarization configuration. Mössbauer spectroscopy showed that there are three different doublets (D1−D3) existing in three FeNSC catalysts, corresponding to low spin (LS) Fe^{3+} (D1: X–Fe^{3+}N–Y), high spin (HS) Fe^{2+} (D2: $Fe^{2+}N_4$) and high spin (HS) Fe^{2+} (D3: X–Fe^{2+}N–Y), respectively (X and Y refer to S and C). Among them, Fe_1-$NS_{1.3}$C possessed more D1 moiety which had been proven to be active for ORR (Fig. 11b). In order to clarify the active sites of Fe_1–$NS_{1.3}$C for ORR, in-situ Mössbauer spectroscopy was performed in O_2-saturated 0.1 M KOH at room temperature (Fig. 11a). As shown in Fig. 11c, the D1 content decreased as the D3 content increased at the potential of 0.85 V (vs. RHE), indicating conversion of spin state from LS Fe^{3+} to HS Fe^{2+}. At the potential of 0.65 V (vs. RHE), the D1 content decreased as the D2 content increased, indicating conversion of spin state from LS Fe^{3+} to HS Fe^{2+}. While at the potential of 0.45 V (vs. RHE), both the D1 and D3 content decreased as the D2 content increased, implying LS Fe^{3+} and HS Fe^{2+} both acted as active sites. Combined with the results that the LS Fe^{3+} still converted into HS Fe^{2+} at the same potential without the existence of O_2, it is proved that D1 active site is sensitive to O_2 molecules and the LS Fe^{3+} of

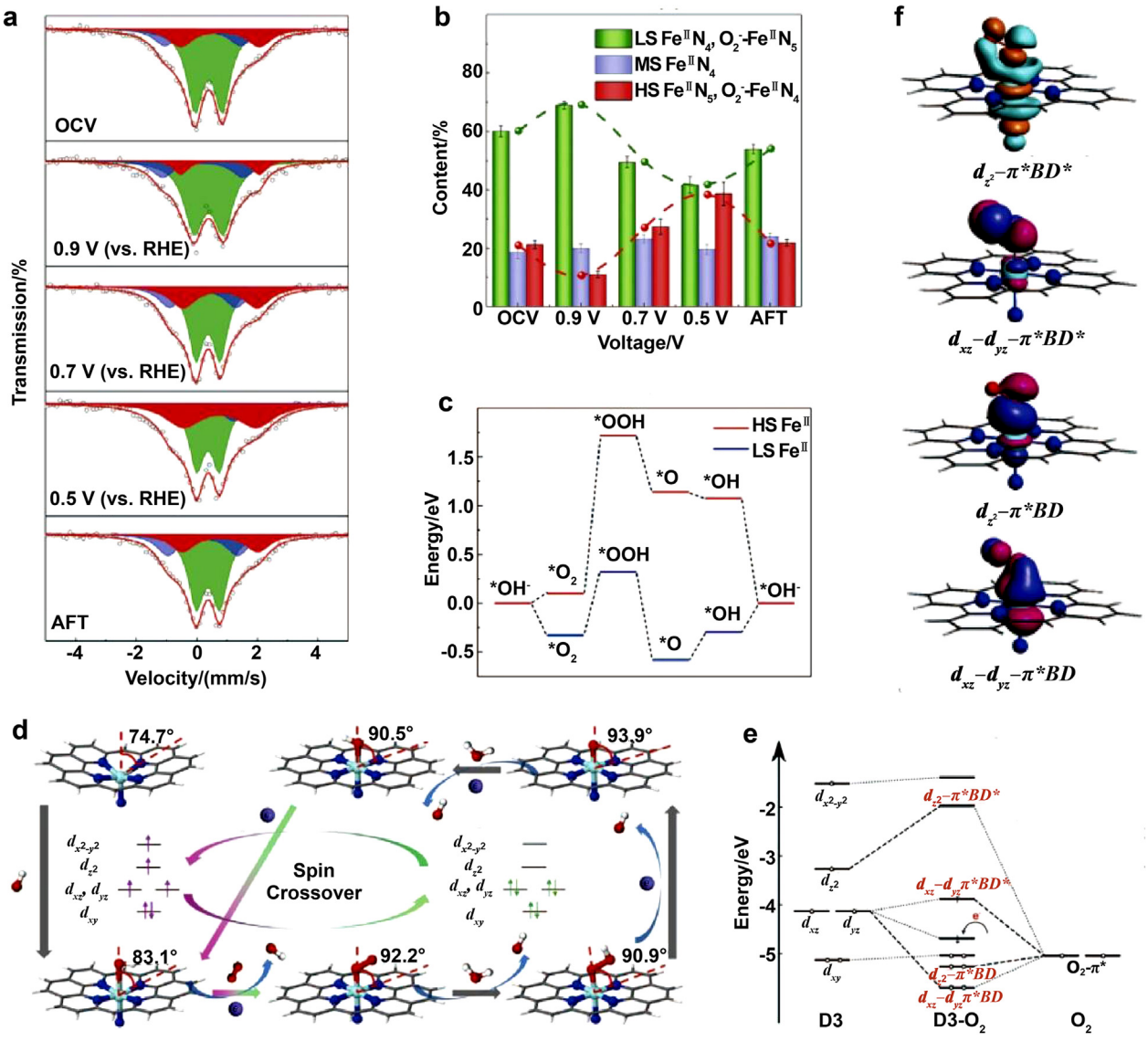

Fig. 10. (a) Operando ^{57}Fe Mössbauer spectra for ^{57}Fe enriched Fe-NC-S recorded at an open-circuit voltage (OCV), 0.9, 0.7, 0.5 V (vs RHE), and after ORR (AFT) in O_2-saturated 1 M KOH at room temperature. (b) Content of different Fe moieties and reactive intermediates at various biases obtained from operando ^{57}Fe Mössbauer measurements. (c) Potential energy profiles of the N–FeN_4C_{10} moiety during ORR in alkaline medium at $U = 0.401$ V. (d) Structural and dynamics of N–FeN_4C_{10} moiety in ORR with optimized geometries. (e) Orbital interactions between O_2 and the N–FeN_4C_{10} moiety. (f) Natural localized molecular orbitals graph of the interactions between O_2 and the N–FeN_4C_{10} moiety. Reproduced with permission from Ref. 74.

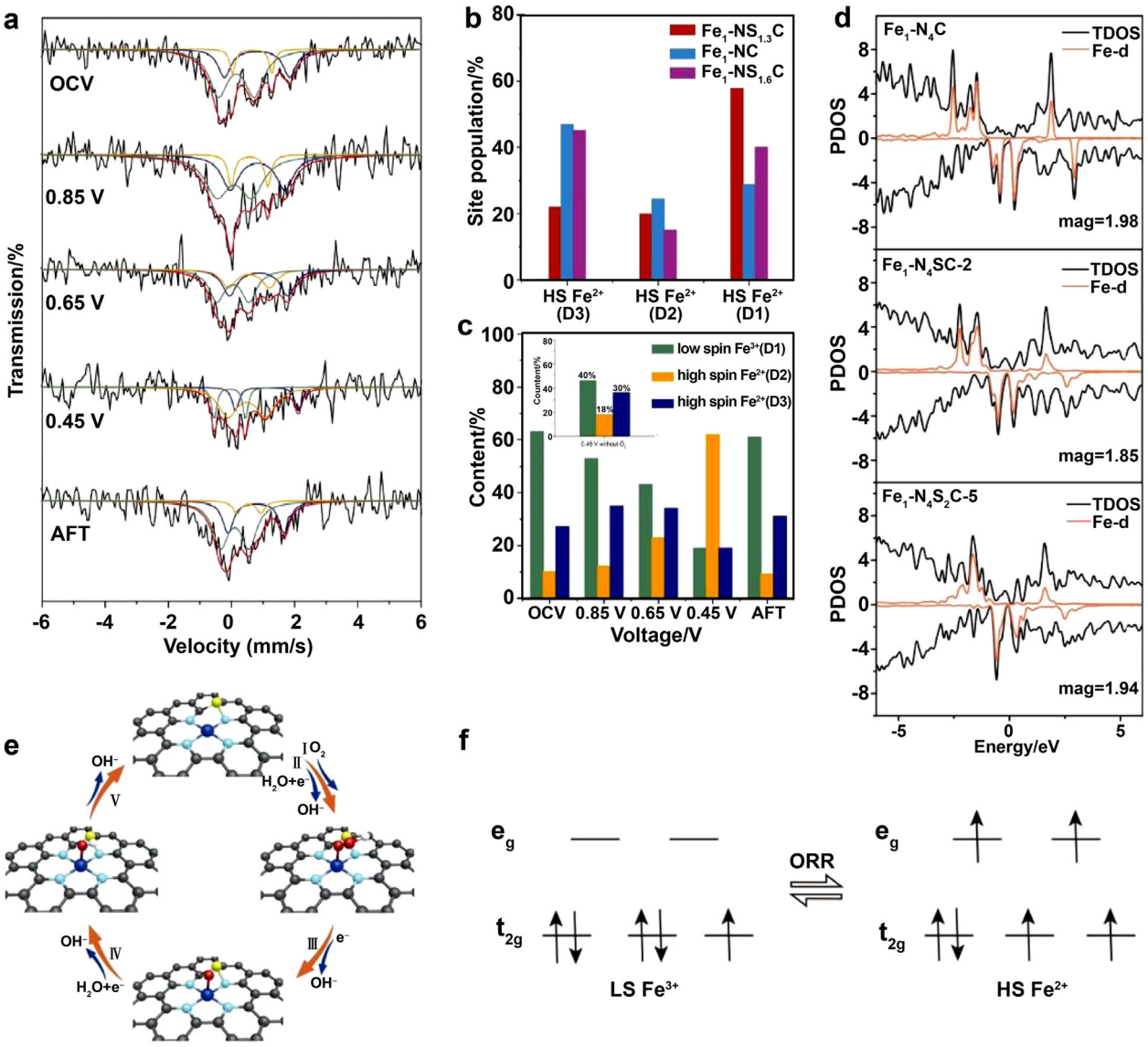

Fig. 11. (a) Operando ^{57}Fe Mössbauer spectra for Fe_1-$NS_{1.3}C$ at open-circuit voltage (OCV), 0.85, 0.65, 0.45 V (vs. RHE), and after ORR (AFT) in O_2-saturated 0.1 M KOH at room temperature. (b) Content of different Fe moieties of the three catalysts. (c) In situ ^{57}Fe Mössbauer spectra at various biases of different Fe moieties and reactive intermediates; Mössbauer spectra at 0.45 V (vs. RHE) without the flux of O_2 (inset). (d) Projected density of states of the Fe center in pristine Fe_1–N_4C, Fe_1–N_4SC-2 and Fe_1–N_4S_2C-5. (e) Proposed ORR mechanism for the Fe_1–N_4SC. (f) Reciprocal transition of spin states during ORR for the Fe_1–N_4SC. Reproduced with permission from Ref. 115.

C–FeN_4–S moiety could be the active site for Fe_1-$NS_{1.3}C$ catalyst in alkaline ORR. DFT indicated that the doping of S impacted the spin polarization and adjusted the spin state of Fe center, resulting in the decrease of the adsorption free energy of *OH, which is further enhanced the activity of ORR (Fig. 11d–f).[115]

Additionally, Zhang et al. designed dual-metal atomically dispersed Fe,Mn/N–C catalyst and revealed that the reduction of oxygen occurred preferentially on Fe(III) in the intermediate spin state.[122] The analysis of Mössbauer spectroscopy and DFT calculation proved that the implant of Mn–N moieties led to Fe(III) 3d electron delocalization and caused the spin state of Fe(III) transition from low spin ($t_{2g}5e_g0$) to intermediate spin ($t_{2g}4e_g1$), which easily penetrated the antibonding π-orbitals of oxygen. Similarly, Zhai et al. found that the introduce of Se could also tune charge redistribution and the spin-state of Fe active sites to improve the electrochemical performance for ORR.[116] Guo et al. introduced $Ti_3C_2T_x$ as the support of iron phthalocyanine (FePc) and achieved a significant enhancement of ORR activity. Temperature-dependent magnetic susceptibility measurement results unveiled that the introduction of $Ti_3C_2T_x$ weakened the paramagnetic state of FeN_4 moieties and increased the number of unpaired d electron of Fe(II) ions, such that more occupied 3d electrons were easily transferred to antibonding π-orbital of oxygen. Compared to the pristine FePc, an additional D1 doublet appeared in the Mössbauer spectrum of the $Ti_3C_2T_x$-supported FePc, belonging to high spin Fe(II). These evidence suggested that van Der Waals forces or hydrogen bonding between FeN_4 moieties and $Ti_3C_2T_x$ induced electron density redistribution and spin-state transition and electron configuration transition from $d_{xy}2d_{yz}1d_{xz}1d_{z^2}1d_{x^2-y^2}1$ to $d_{xy}2d_{yz}2d_{xz}1d_{z^2}1$ was thought to be responsible for the enhanced ORR activity through yielding an easier dioxygen adsorption and reduction.[117]

4.3.2. *Oxygen reduction reaction (O_2→H_2O_2)*

Hydrogen peroxide is a versatile chemical, however, its industrial synthesis involves an energy intensive and tedious anthraquinone process.[123] Therefore, the synthesis of hydrogen peroxide by ORR offers a simpler and more sustainable approach to tackle this challenge. The production of H_2O_2 via $2e^-$ ORR involves two proton-coupled electron

transfer steps:

$$* + O_2 + H^+ + e^- \rightarrow *OOH \quad (1)$$

$$*OOH + H^+ + e^- \rightarrow H_2O_2 + * \quad (2)$$

Liu et al. proved that Fe–N–C adsorbed OOH* so strongly that the selectivity of H_2O_2 is low.[124] Although the Fe–N–C has poor selectivity for hydrogen peroxide, the selectivity can be improved after doping and other treatments due to the modification of metal center. Xue et al. prepared a cheap sodium ferric EDTA-derived material (EDTAFe-Na-KB-HT1), an iron and nitrogen co-doped Fe–N–C catalyst with micro-mesoporous structure and large surface area via one-step pyrolysis. The catalyst exhibited high selectivity (80%–100%) towards H_2O_2 with a large current density.[125] Choi et al. used H_2O_2 to introduce oxygen functional groups to the carbon surface of Fe–N–C, which changed the reaction path of ORR and led to a 30% increase towards H_2O_2.[126] Yagi et al. synthesized Cu-, Fe-, and N-doped carbon nanotubes, (Cu, Fe)–N-CNT as an ORR catalyst. It showed a high selectivity of 99% towards H_2O_2. Kinetic analysis revealed that the rate constant for the reduction of O_2 to H_2O_2 is two orders of magnitude higher than that for the reduction of O_2 to H_2O.[127] Besides, H_2O_2 could be trapped in the micropores of powders and further reduced to H_2O. Therefore, constructing a free-standing SACs electrode could prevent the further reduction of H_2O_2 and improve the selectivity.

5. Summary, challenges and outlook

In summary, we concluded common methods for the preparation of Fe–N–C single-atom catalysts, including high-temperature pyrolysis, chemical vapor decomposition (CVD) and ball milling. Then, the relationship between the electronic structure of Fe single atoms and spin configurations is outlined, and based on this, the common methods of spin regulation are briefly mentioned, and the electronic structure of Fe and the orbital coupling of C, N and O are summarized. Finally, the application of Fe–N–C in electrocatalytic C, N and O conversion is introduced, including CO_2RR, NRR, NitRR and ORR. Here, we would like to present the challenges and outlook of Fe–N–C, which may provide some opportunities for the future development of SACs.

(1) The loadings of catalysts synthesized with the existing methods are still not high, so it becomes an important task to find more reasonable and effective means to synthesize catalysts with high site densities. It should not be overlooked that the increase in loading can cause inferior mass transfer, thus the structural design of the catalyst is particularly important.
(2) A reasonable Fe–N bond length can effectively prevent the aggregation of iron atoms and increase the stability of the active sites. However, there is a lack of study in such topic. More efforts shall be devoted to exploring the relationship between catalyst structure and reaction performance from a smaller scale.
(3) The structures of SACs do not maintain unchanged during the reactions. Therefore, it is important to develop new techniques to achieve in situ characterization of catalysts to disclose the underlying mechanism and discover better catalysts.
(4) The spin regulation of Fe–N–C by external experimental conditions is seldom studied at present. For example, the modification of catalytic properties by applying a magnetic field in the electrocatalytic process has not received enough attention.
(5) The spin regulation of Fe–N–C by changing prepared conditions remains to be further developed. Although many reports expounded temperature, heteroatom doping, and other factors can change the spin state of the iron center, the mechanism is not clearly explained. In addition, it is unknown whether some conditions such as the applied magnetic field will exert an effect on the spin state.
(6) DFT calculations were reasonably used to predict the spin electron transfer trends on different reactions of Fe–N–C prepared under different conditions. Proper utilization of the DFT calculations can lead to suitable thermodynamic data,[128,129] such as adsorption energy, dissociation energy and splitting energy, which may provide new possibilities for the design of Fe–N–C catalysts and mechanistic explanations.

Declaration of competing interest

The authors declare that they have no known competing financial interests or personal relationships that could have appeared to influence the work reported in this paper.

Acknowledgements

We are grateful for the financial support from National Natural Science Foundation of China (No. 21974103) and the start-up funds of Wuhan University.

References

1. Debe MK. Electrocatalyst approaches and challenges for automotive fuel cells. *Nature*. 2012;486:43–51.
2. Chu S, Majumdar A. Opportunities and challenges for a sustainable energy future. *Nature*. 2012;488:294–303.
3. Tian XL, Lu XF, Xia BY, et al. Advanced electrocatalysts for the oxygen reduction reaction in energy conversion technologies. *Joule*. 2020;4:45–68.
4. Jiao Y, Zheng Y, Jaroniec MT, et al. Design of electrocatalysts for oxygen- and hydrogen-involving energy conversion reactions. *Chem Soc Rev*. 2015;44:2060–2086.
5. Yang CL, Wang LN, Yin P, et al. Sulfur-anchoring synthesis of platinum intermetallic nanoparticle catalysts for fuel cells. *Science*. 2021;374:459–464.
6. Seh ZW, Kibsgaard J, Dickens CF, et al. Combining theory and experiment in electrocatalysis: insights into materials design. *Science*. 2017;355:4998.
7. Yang Y, Peltier CR, Zeng R, et al. Electrocatalysis in alkaline media and alkaline membrane-based energy technologies. *Chem Rev*. 2022;122:6117–6321.
8. Corma A, Concepción P, Boronat M, et al. Exceptional oxidation activity with size-controlled supported gold clusters of low atomicity. *Nat Chem*. 2013;5:775–781.
9. Liu Y, Tsunoyama H, Akita T, et al. Aerobic oxidation of cyclohexane catalyzed by size-controlled au clusters on hydroxyapatite: size effect in the sub-2 nm regime. *ACS Catal*. 2011;1:2–6.
10. Chen Y, Ji S, Chen C, et al. Single-atom catalysts: synthetic strategies and electrochemical applications. *Joule*. 2018;2:1242–1264.
11. Zhang B, Zheng X, Voznyy O, et al. Homogeneously dispersed multimetal oxygen-evolving catalysts. *Science*. 2016;352:333–337.
12. Chen F, Jiang X, Zhang L, et al. Single-atom catalysis: bridging the homo- and heterogeneous catalysis. *Chin J Catal*. 2018;39:893–898.
13. Liu P, Zhao Y, Qin R, et al. Photochemical route for synthesizing atomically dispersed palladium catalysts. *Science*. 2016;352:797–800.
14. Ji S, Chen Y, Wang X, et al. Chemical synthesis of single atomic site catalysts. *Chem Rev*. 2020;120:11900–11955.
15. Qiao B, Wang A, Yang X, et al. Single-atom catalysis of CO oxidation using Pt_1/FeO_x. *Nat Chem*. 2011;3:634–641.
16. Liu W, Cao LL, Cheng WR, et al. Single-site active cobalt-based photocatalyst with a long carrier lifetime for spontaneous overall water splitting. *Angew Chem Int Ed*. 2017;56:9312–9317.
17. Wang YB, Zhao X, Cao D, et al. Peroxymonosulfate enhanced visible light photocatalytic degradation bisphenol A by single-atom dispersed Ag mesoporous g-C_3N_4 hybrid. *Appl Catal, B*. 2017;211:79–88.
18. Fang XZ, Shang QC, Wang Y, et al. Single Pt atoms confined into a metal-organic framework for efficient photocatalysis. *Adv Mater*. 2018;30, 1705112.
19. Zuo Q, Liu TT, Chen CS, et al. Ultrathin metal-organic framework nanosheets with ultrahigh loading of single pt atoms for efficient visible-light-driven photocatalytic H_2 evolution. *Angew Chem Int Ed*. 2019;58:10198–10203.
20. Gao C, Low JX, Long R, et al. Heterogeneous single-atom photocatalysts: fundamentals and applications. *Chem Rev*. 2020;120:12175–12216.
21. Yin PQ, Yao T, Wu Y, et al. Single cobalt atoms with precise N-coordination as superior oxygen reduction reaction catalysts. *Angew Chem Int Ed*. 2016;55:10800–10805.
22. Chen JY, Li H, Fan C, et al. Dual single-atomic $Ni-N_4$ and $Fe-N_4$ sites constructing janus hollow graphene for selective oxygen electrocatalysis. *Adv Mater*. 2020;32, 2003134.
23. Zhang Q, Guan J. Single-atom catalysts for electrocatalytic applications. *Adv Funct Mater*. 2020;30, 2000768.
24. Ren X, Liu S, Li H, et al. Electron-withdrawing functional ligand promotes CO_2 reduction catalysis in single atom catalyst. *Sci China Chem*. 2020;63:1727–1733.
25. Yang HB, Hung SF, Liu S, et al. Atomically dispersed Ni(I) as the active site for electrochemical CO_2 reduction. *Nat Energy*. 2018;3:140–147.

26. Zhao YX, Li ZY, Yuan Z, et al. Thermal methane conversion to formaldehyde promoted by single platinum atoms in $PtAl_2O_4^-$ cluster anions. *Angew Chem Int Ed*. 2014;53:9482–9486.
27. Yan H, Cheng H, Yi H, et al. Single-atom Pd_1/graphene catalyst achieved by atomic layer deposition: remarkable performance in selective hydrogenation of 1,3-butadiene. *J Am Chem Soc*. 2015;137:10484–10487.
28. Chen ZP, Vorobyeva E, Mitchell S, et al. A heterogeneous single-atom palladium catalyst surpassing homogeneous systems for Suzuki coupling. *Nat Nanotechnol*. 2018;13:702–704.
29. Yang XF, Wang A, Qiao B, et al. Single-atom catalysts: a new frontier in heterogeneous catalysis. *Acc Chem Res*. 2013;46:1740–1748.
30. Zhang J, Ma J, Choksi TS, et al. Strong metal–support interaction boosts activity, selectivity, and stability in electrosynthesis of H_2O_2. *J Am Chem Soc*. 2022;144:2255–2263.
31. Wang Q, Zhao ZL, Dong S, et al. Design of active nickel single-atom decorated MoS_2 as a pH-universal catalyst for hydrogen evolution reaction. *Nano Energy*. 2018;53:458–467.
32. Han GF, Li F, Rykov AI, et al. Abrading bulk metal into single atoms. *Nat Nanotechnol*. 2022;17:403–407.
33. Kyriakou G, Boucher MB, Jewell AD, et al. Isolated metal atom geometries as a strategy for selective heterogeneous hydrogenations. *Science*. 2012;335:1209–1212.
34. He T, Chen SM, Ni B, et al. Zirconium-porphyrin-based metal-organic framework hollow nanotubes for immobilization of noble-metal single atoms. *Angew Chem Int Ed*. 2018;57:3493–3498.
35. Zhu T, Chen Q, Liao P, et al. Single-atom Cu catalysts for enhanced electrocatalytic nitrate reduction with significant alleviation of nitrite production. *Small*. 2020;16,2004526.
36. Zhou Y, Yu YN, Ma DS, et al. Atomic Fe dispersed hierarchical mesoporous Fe-N-C nanostructures for an efficient oxygen reduction reaction. *ACS Catal*. 2021;11:74–81.
37. Zhang LW, Long R, Zhang YM, et al. Direct observation of dynamic bond evolution in single-atom Pt/C_3N_4 catalysts. *Angew Chem Int Ed*. 2020;59:6224–6229.
38. An SF, Zhang GH, Wang TW, et al. High-density ultra-small clusters and single-atom Fe sites embedded in graphitic carbon nitride (g-C_3N_4) for highly efficient catalytic advanced oxidation processes. *ACS Nano*. 2018;12:9441–9450.
39. Elibol K, Mangler C, O'regan DD, et al. Single indium atoms and few-atom indium clusters anchored onto graphene via silicon heteroatoms. *ACS Nano*. 2021;15:14373–14383.
40. Fei H, Dong J, Chen D, et al. Single atom electrocatalysts supported on graphene or graphene-like carbons. *Chem Soc Rev*. 2019;48:5207–5241.
41. Karapinar D, Huan NT, Sahraie NR, et al. Electroreduction of CO_2 on single-site copper-nitrogen-doped carbon material: selective formation of ethanol and reversible restructuration of the metal sites. *Angew Chem Int Ed*. 2019;58:15098–15103.
42. Möller T, Ju W, Bagger A, et al. Efficient CO_2 to CO electrolysis on solid Ni–N–C catalysts at industrial current densities. *Energy Environ Sci*. 2019;12:640–647.
43. Ju W, Bagger A, Wang X, et al. Unraveling mechanistic reaction pathways of the electrochemical CO_2 reduction on Fe–N–C single-site catalysts. *ACS Energy Lett*. 2019;4:1663–1671.
44. Bi W, Li X, You R, et al. Surface immobilization of transition metal ions on nitrogen-doped graphene realizing high-efficient and selective CO_2 reduction. *Adv Mater*. 2018;30, 1706617.
45. Zhao W, Zhang L, Luo Q, et al. Single $Mo_1(Cr_1)$ atom on nitrogen-doped graphene enables highly selective electroreduction of nitrogen into ammonia. *ACS Catal*. 2019;9:3419–3425.
46. Wang M, Liu S, Qian T, et al. Over 56.55% faradaic efficiency of ambient ammonia synthesis enabled by positively shifting the reaction potential. *Nat Commun*. 2019;10:341.
47. Li J, Chen S, Yang N, et al. Ultrahigh-loading zinc single-atom catalyst for highly efficient oxygen reduction in both acidic and alkaline media. *Angew Chem Int Ed*. 2019;58:7035–7039.
48. Xiao F, Xu GL, Sun CJ, et al. Nitrogen-coordinated single iron atom catalysts derived from metal organic frameworks for oxygen reduction reaction. *Nano Energy*. 2019;61:60–68.
49. Ding J, Huang J, Zhang Q, et al. A hierarchical monolithic cobalt-single-atom electrode for efficient hydrogen peroxide production in acid. *Catal Sci Technol*. 2022;12:2416–2419.
50. Sun XP, Sun SX, Gu SQ, et al. High-performance single atom bifunctional oxygen catalysts derived from ZIF-67 superstructures. *Nano Energy*. 2019;61:245–250.
51. Ma M, Li G, Yan W, et al. Single-atom molybdenum engineered platinum nanocatalyst for boosted alkaline hydrogen oxidation. *Adv Energy Mater*. 2022;12,2103336.
52. Chen WX, Pei JJ, He CT, et al. Rational design of single molybdenum atoms anchored on N-doped carbon for effective hydrogen evolution reaction. *Angew Chem Int Ed*. 2017;56:16086–16090.
53. Liu B, Shioyama H, Akita T, et al. Metal-organic framework as a template for porous carbon synthesis. *J Am Chem Soc*. 2008;130:5390–5391.
54. Wei YS, Zhang M, Zou R, et al. Metal–organic framework-based catalysts with single metal sites. *Chem Rev*. 2020;120:12089–12174.
55. Chen X, Ma DD, Chen B, et al. Metal-organic framework-derived mesoporous carbon nanoframes embedded with atomically dispersed Fe-N_x active sites for efficient bifunctional oxygen and carbon dioxide electroreduction. *Appl Catal, B*. 2020;267, 118720.
56. Xie XY, Peng LS, Yang HZ, et al. MIL-101-derived mesoporous carbon supporting highly exposed Fe single-atom sites as efficient oxygen reduction reaction catalysts. *Adv Mater*. 2021;33, 2101038.
57. Jiao L, Zhang R, Wan G, et al. Nanocasting SiO_2 into metal-organic frameworks imparts dual protection to high-loading Fe single-atom electrocatalysts. *Nat Commun*. 2020;11:2831.
58. Hu LY, Dai CL, Chen LW, et al. Metal-triazolate-framework-derived FeN_4Cl_1 single-atom catalysts with hierarchical porosity for the oxygen reduction reaction. *Angew Chem Int Ed*. 2021;60:27324–27329.
59. Al-Zoubi T, Zhou Y, Yin X, et al. Preparation of nonprecious metal electrocatalysts for the reduction of oxygen using a low-temperature sacrificial metal. *J Am Chem Soc*. 2020;142:5477–5481.
60. Jiao L, Wan G, Zhang R, et al. From metal-organic frameworks to single-atom Fe implanted N-doped porous carbons: efficient oxygen reduction in both alkaline and acidic media. *Angew Chem Int Ed*. 2018;57:8525–8529.
61. Chen Y, Li Z, Zhu Y, et al. Atomic Fe dispersed on N-doped carbon hollow nanospheres for high-efficiency electrocatalytic oxygen reduction. *Adv Mater*. 2019;31, 1806312.
62. Miao ZP, Wang XM, Zhao ZL, et al. Improving the stability of non-noble-metal M-N-C catalysts for proton-exchange-membrane fuel cells through M-N bond length and coordination regulation. *Adv Mater*. 2021;33, 2006613.
63. Liu SW, Wang MY, Yang XX, et al. Chemical vapor deposition for atomically dispersed and nitrogen coordinated single metal site catalysts. *Angew Chem Int Ed*. 2020;59:21698–21705.
64. Wang J, Li B, Li Y, et al. Facile synthesis of atomic Fe-N-C materials and dual roles investigation of Fe-N_4 sites in Fenton-like reactions. *Adv Sci*. 2021;8, 2101824.
65. Li X, Yang X, Liu L, et al. Chemical vapor deposition for N/S-doped single fe site catalysts for the oxygen reduction in direct methanol fuel cells. *ACS Catal*. 2021;11:7450–7459.
66. Gao Y, Duan XG, Li B, et al. Fe containing template derived atomic Fe-N-C to boost Fenton-like reaction and charge migration analysis on highly active Fe-N-4 sites. *J Mater Chem*. 2021;9:14793–14805.
67. Jiao L, Li J, Richard LL, et al. Chemical vapour deposition of Fe-N-C oxygen reduction catalysts with full utilization of dense Fe-N_4 sites. *Nat Mater*. 2021;20:1385–1391.
68. Xing L, Jin Y, Weng Y, et al. Top-down synthetic strategies toward single atoms on the rise. *Matter*. 2022;5:788–807.
69. Wang X, Ding S, Yue T, et al. Universal domino reaction strategy for mass production of single-atom metal-nitrogen catalysts for boosting CO_2 electroreduction. *Nano Energy*. 2021;82, 105689.
70. Deng D, Chen X, Yu L, et al. A single iron site confined in a graphene matrix for the catalytic oxidation of benzene at room temperature. *Sci Adv*. 2015;1, 1500462.
71. Cui X, Xiao J, Wu Y, et al. A graphene composite material with single cobalt active sites: a highly efficient counter electrode for dye-sensitized solar cells. *Angew Chem Int Ed*. 2016;55:6708–6712.
72. Zhou J, Duchesne PN, Hu Y, et al. Fe-N bonding in a carbon nanotube–graphene complex for oxygen reduction: an XAS study. *Phys Chem Chem Phys*. 2014;16:15787–15791.
73. Thole BT, Van Der Laan G, Butler PH. Spin-mixed ground state of Fe phthalocyanine and the temperature-dependent branching ratio in X-ray absorption spectroscopy. *Chem Phys Lett*. 1988;149:295–299.
74. Li X, Cao CS, Hung SF, et al. Identification of the electronic and structural dynamics of catalytic centers in single-Fe-atom material. *Chem*. 2020;6:3440–3454.
75. Li X, Zeng Y, Tung CW, et al. Unveiling the in situ generation of a monovalent Fe(I) site in the single-fe-atom catalyst for electrochemical CO_2 reduction. *ACS Catal*. 2021;11:7292–7301.
76. Li X, Zhu K, Pang J, et al. Unique role of Mössbauer spectroscopy in assessing structural features of heterogeneous catalysts. *Appl Catal, B*. 2018;224:518–532.
77. Li J, Sougrati MT, Zitolo A, et al. Identification of durable and non-durable FeN_x sites in Fe-N-C materials for proton exchange membrane fuel cells. *Nat Catal*. 2021;4:10–19.
78. Saha P, Amanullah S, Dey A. Selectivity in electrochemical CO_2 reduction. *Acc Chem Res*. 2022;55:134–144.
79. Wang S, Li B, Li L, et al. Highly efficient N_2 fixation catalysts: transition-metal carbides M_2C (MXenes). *Nanoscale*. 2020;12:538–547.
80. Wang Y, Cheng W, Yuan P, et al. Boosting nitrogen reduction to ammonia on FeN_4 sites by atomic spin regulation. *Adv Sci*. 2021;8, 2102915.
81. Wang XT, Ouyang T, Wang L, et al. Redox-inert Fe^{3+} ions in octahedral sites of Co-Fe spinel oxides with enhanced oxygen catalytic activity for rechargeable zinc–air batteries. *Angew Chem Int Ed*. 2019;58:13291–13296.
82. Wang H, Liu R, Li Y, et al. Durable and efficient hollow porous oxide spinel microspheres for oxygen reduction. *Joule*. 2018;2:337–348.
83. Zhang JC, Cai WZ, Hu FX, et al. Recent advances in single atom catalysts for the electrochemical carbon dioxide reduction reaction. *Chem Sci*. 2021;12:6800–6819.
84. Gu J, Hsu CS, Bai L, et al. Atomically dispersed Fe^{3+} sites catalyze efficient CO_2 electroreduction to CO. *Science*. 2019;364:1091–1094.
85. Chen S, Li X, Kao CW, et al. Unveiling the proton-feeding effect in sulfur-doped Fe-N-C single-atom catalyst for enhanced CO_2 electroreduction. *Angew Chem Int Ed*. 2022, e202206233.
86. Chen Y, Li G, Zeng Y, et al. Boosting faradaic efficiency of CO_2 electroreduction to CO for Fe−N−C single-site catalysts by stabilizing Fe^{3+} sites via F-doping. *Nano Res*. 2022. https://doi.org/10.1007/s12274-022-4441-0.
87. Li K, Zhang S, Zhang X, et al. Atomic tuning of single-atom Fe-N-C catalysts with phosphorus for robust electrochemical CO_2 reduction. *Nano Lett*. 2022;22:1557–1565.
88. Li Z, Wu R, Xiao S, et al. Axial chlorine coordinated iron-nitrogen-carbon single-atom catalysts for efficient electrochemical CO_2 reduction. *Chem Eng J*. 2022;430,132882.

89. Xie YX, Liu N, Li X, et al. The Influence of single-atom $Fe^{2+/3+}N_4$ spin state on the electroreduction of CO_2 to CO/HCOOH by analyzing proton/electron transfer mechanisms and free energy evolutions. *J Phys Chem C*. 2021;125:21460–21470.
90. Wang Y, Cui X, Zhao J, et al. Rational design of Fe-N/C hybrid for enhanced nitrogen reduction electrocatalysis under ambient conditions in aqueous solution. *ACS Catal*. 2019;9:336–344.
91. Lü F, Zhao S, Guo R, et al. Nitrogen-coordinated single Fe sites for efficient electrocatalytic N_2 fixation in neutral media. *Nano Energy*. 2019;61:420–427.
92. He C, Wu ZY, Zhao L, et al. Identification of FeN_4 as an efficient active site for electrochemical N_2 reduction. *ACS Catal*. 2019;9:7311–7317.
93. Wu ZY, Karamad M, Yong X, et al. Electrochemical ammonia synthesis via nitrate reduction on Fe single atom catalyst. *Nat Commun*. 2021;12:2870.
94. Li P, Jin Z, Fang Z, et al. A single-site iron catalyst with preoccupied active centers that achieves selective ammonia electrosynthesis from nitrate. *Energy Environ Sci*. 2021;14:3522–3531.
95. Li J, Li M, An N, et al. Atomically dispersed Fe atoms anchored on S and N-codoped carbon for efficient electrochemical denitrification. *Proc Natl Acad Sci USA*. 2021;118, e2105628118.
96. Murphy E, Liu Y, Matanovic I, et al. Highly durable and selective Fe- and Mo-based atomically dispersed electrocatalysts for nitrate reduction to ammonia via distinct and synergized NO_2^- pathways. *ACS Catal*. 2022;12:6651–6662.
97. Erisman JW, Sutton MA, Galloway J, et al. How a century of ammonia synthesis changed the world. *Nat Geosci*. 2008;1:636–639.
98. Galloway JN, Townsend AR, Erisman JW, et al. Transformation of the nitrogen cycle: recent trends, questions, and potential solutions. *Science*. 2008;320:889–892.
99. Liu QL, Wang YF, Hu ZZ, et al. Iron-based single-atom electrocatalysts: synthetic strategies and applications. *RSC Adv*. 2021;11:3079–3095.
100. Zhang R, Jiao L, Yang W, et al. Single-atom catalysts templated by metal-organic frameworks for electrochemical nitrogen reduction. *J Mater Chem*. 2019;7:26371–26377.
101. Singh AR, Rohr BA, Schwalbe JA, et al. Electrochemical ammonia synthesis—the selectivity challenge. *ACS Catal*. 2017;7:706–709.
102. Li XF, Li QK, Cheng J, et al. Conversion of dinitrogen to ammonia by FeN_3-embedded graphene. *J Am Chem Soc*. 2016;138:8706–8709.
103. Song G, Gao R, Zhao Z, et al. High-spin state Fe(III) doped TiO_2 for electrocatalytic nitrogen fixation induced by surface F modification. *Appl Catal, B*. 2022;301, 120809.
104. Mauter MS, Fiske PS. Desalination for a circular water economy. *Energy Environ Sci*. 2020;13:3180–3184.
105. Xu H, Ma Y, Chen J, et al. Electrocatalytic reduction of nitrate—a step towards a sustainable nitrogen cycle. *Chem Soc Rev*. 2022;51:2710–2758.
106. Wang Y, Xu A, Wang Z, et al. Enhanced nitrate-to-ammonia activity on copper-nickel alloys via tuning of intermediate adsorption. *J Am Chem Soc*. 2020;142:5702–5708.
107. Martínez J, Ortiz A, Ortiz I. State-of-the-art and perspectives of the catalytic and electrocatalytic reduction of aqueous nitrates. *Appl Catal, B*. 2017;207:42–59.
108. Jiao K, Xuan J, Du Q, et al. Designing the next generation of proton-exchange membrane fuel cells. *Nature*. 2021;595:361–369.
109. Wang J, Ding W, Wei ZD. Performance of polymer electrolyte membrane fuel cells at ultra-low platinum loadings. *Acta Phys Chim Sin*. 2021;37, 2009094.
110. Yang XD, Chen C, Zhou ZY, et al. Advances in active site structure of carbon-based non-precious metal catalysts for oxygen reduction reaction. *Acta Phys Chim Sin*. 2019;35:472–485.
111. Zhang J, Yang H, Liu B. Coordination engineering of single-atom catalysts for the oxygen reduction reaction: a review. *Adv Energy Mater*. 2021;11, 2002473.
112. Yang J, Li JF, Ding RM, et al. Kinetic effects of temperature on Fe-N-C catalysts for $2e^-$ and $4e^-$ oxygen reduction reactions. *J Electrochem Soc*. 2021;168, 096502.
113. Snitkoff-Sol RZ, Friedman A, Honig HC, et al. Quantifying the electrochemical active site density of precious metal-free catalysts in situ in fuel cells. *Nature Catal*. 2022;5:163–170.
114. Kumar K, Dubau L, Mermoux M, et al. On the influence of oxygen on the degradation of Fe-N-C catalysts. *Angew Chem Int Ed*. 2020;59:3235–3243.
115. Chen Z, Niu H, Ding J, et al. Unraveling the origin of sulfur-doped Fe-N-C single atom catalyst for enhanced oxygen reduction activity: effect of Fe-spin state tuning. *Angew Chem Int Ed*. 2021;60:25404–25410.
116. Chen Z, Su X, Ding J, et al. Boosting oxygen reduction reaction with Fe and Se dual-atom sites supported by nitrogen-doped porous carbon. *Appl Catal, B*. 2022;308, 121206.
117. Sun Y, Sun S, Yang H, et al. Spin-related electron transfer and orbital interactions in oxygen electrocatalysis. *Adv Mater*. 2020;32, 2003297.
118. Han J, Bao H, Wang JQ, et al. 3D N-doped ordered mesoporous carbon supported single-atom Fe-N-C catalysts with superior performance for oxygen reduction reaction and zinc-air battery. *Appl Catal, B*. 2021;280, 119411.
119. Peng L, Yang J, Yang Y, et al. Mesopore-rich Fe-N-C catalyst with FeN_4-O-NC single-atom sites delivers remarkable oxygen reduction reaction performance in alkaline media. *Adv Mater*. 2022, 2202544.
120. Xie X, Shang L, Xiong X, et al. Fe single-atom catalysts on MOF-5 derived carbon for efficient oxygen reduction reaction in proton exchange membrane fuel cells. *Adv Energy Mater*. 2022;12, 2102688.
121. Zhou Y, Chen G, Wang Q, et al. Fe-N-C electrocatalysts with densely accessible Fe-N_4 sites for efficient oxygen reduction reaction. *Adv Funct Mater*. 2021;31, 2102420.
122. Yang G, Zhu J, Yuan P, et al. Regulating Fe-spin state by atomically dispersed Mn-N in Fe-N-C catalysts with high oxygen reduction activity. *Nat Commun*. 2021;12:1734.
123. Zhang JC, Yang HB, Gao JJ, et al. Design of hierarchical, three-dimensional free-standing single-atom electrode for H_2O_2 production in acidic media. *Carbon Energy*. 2020;2:276–282.
124. Liu J, Gong Z, Yan M, et al. Electronic structure regulation of single-atom catalysts for electrochemical oxygen reduction to H_2O_2. *Small*. 2022;18, 2103824.
125. Yan XH, Meng ZW, Liu J, et al. Sodium ferric EDTA-derived Fe-N-C material for selectively electrocatalytic synthesis of hydrogen peroxide. *Mater Lett*. 2018;217:171–173.
126. Suk M, Chung MW, Han MH, et al. Selective H_2O_2 production on surface-oxidized metal-nitrogen-carbon electrocatalysts. *Catal Today*. 2021;359:99–105.
127. Kato M, Fujibayashi N, Abe D, et al. Impact of heterometallic cooperativity of iron and copper active sites on electrocatalytic oxygen reduction kinetics. *ACS Catal*. 2021;11:2356–2365.
128. Gao J, Tao H, Liu B. Progress of nonprecious-metal-based electrocatalysts for oxygen evolution in acidic media. *Adv Mater*. 2021;33, 2003786.
129. Tao HB, Zhang J, Chen J, et al. Revealing energetics of surface oxygen redox from kinetic fingerprint in oxygen electrocatalysis. *J Am Chem Soc*. 2019;141:13803–13811.

Jian Huang obtained his bachelor degree at Wuhan University in 2020. Currently, he is a Master's Degree student at Wuhan University. He focuses on the design of single atom electrocatalysts and their applications toward oxygen reduction reaction and nitrate reduction reaction.

Qiao Zhang obtained her Bachelor of Science degree in Applied Chemistry from Northeastern University in 2019. She is currently working towards a PhD in the Institute for Advanced Studies at Wuhan University. Her doctoral research is focused on single-atom catalysts for small molecule conversion.

Jie Ding received his master's degree (2017) in Chemical Technology from Wuhan Institute of Technology. During 2017–2019, he worked as a joint assistant researcher under the supervision of Prof. Yanqiang Huang at DICP, CAS. He is currently pursuing his Ph.D. at the Institute for Advanced Studies, Wuhan University. His research interest mainly focuses on small molecule activation for energy catalysis applications.

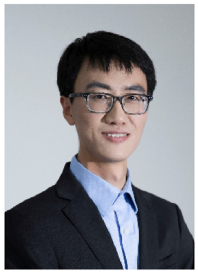

Yueming Zhai obtained his bachelor degree at Jilin University in 2005, and completed his PhD program at Changchun institute of applied chemistry, Chinese academy of sciences in 2012. In 2012–2016, he performed post-doctor research in the department of chemistry at University of Florida. In 2016–2018, he worked as senior fellow in the department of bioengineering at University of Washington. In 2018, he joined the institute for advanced studies, Wuhan University as a professor. His research interests are designing of nanostructures for electrocatalysis and electroanalysis.